J. Fluid Mech. (2023), *vol*. 960, A40, doi:10.1017/jfm.2023.232

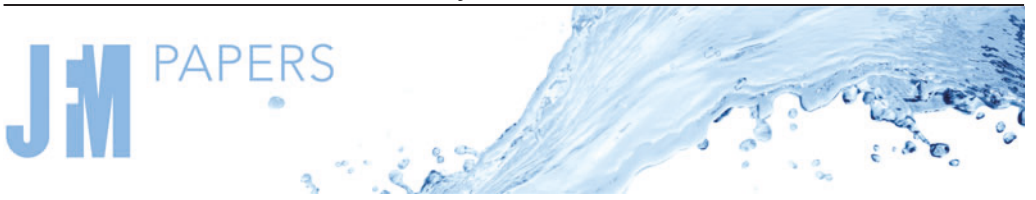

Selection of vortex ripple dimensions in sinusoidal oscillatory flows. Part 1. Ripple dimensions and fluid kinematics

Liangyi Yue[1,2,†], **Tian-Jian Hsu**[2] **and Alexander R. Horner-Devine**[3]

[1]The Bob and Norma Street Environmental Fluid Mechanics Laboratory, Department of Civil and Environmental Engineering, Stanford University, Stanford, CA 94305, USA

[2]Center for Applied Coastal Research, Civil and Environmental Engineering, University of Delaware, Newark, DE 19716, USA

[3]Civil and Environmental Engineering, University of Washington, Seattle, WA 98195, USA

(Received 1 September 2022; revised 5 March 2023; accepted 14 March 2023)

Subaqueous vortex ripples in equilibrium are characterized by their unique geometry and dimensions. Motivated by the recent direct numerical simulation study of oscillatory turbulent flow over a wavy bottom by Önder & Yuan (*J. Fluid Mech.*, vol. 858, 2019, pp. 264–314), the objective of this study is to further investigate the fluid dynamical controls that determine the distinctive equilibrium dimensions of vortex ripples. We use direct numerical simulations to investigate the differences in flow kinetics between sinusoidal oscillatory flow over equilibrium and out-of-equilibrium vortex ripples. In comparison with the equilibrium case, the spanwise coherent vortices, the averaged bottom shear stress on overlying flow and the shear stress distribution on the ripple surface are identified as the key fluid dynamical controls on equilibrium dimensions. Based on these controls, we propose mechanisms in the selection of vortex ripple dimensions. We observe that the flow adjusts in such a way that the interaction between overlying flow and vortex ripples tends to generate the strongest coherent vortices while the ripple surface (or overlying flow) experiences the smallest shear stress averaged over ripple wavelength during the selection process. Through a triple decomposition of the flow, the component of the ripple-induced fluctuation is found to dictate these fluid dynamical controls, which implies that this component plays an important role in the evolution of vortex ripples.

Key words: coastal engineering, vortex shedding, turbulent boundary layers

† Email address for correspondence: liangyi@stanford.edu

1. Introduction

Subaqueous sand ripples are ubiquitous in the coastal ocean (Grant & Madsen 1986; Blondeaux 2001), and hence the study of turbulent oscillatory flow over ripples is of high interest for the understanding of hydrodynamic dissipation and sediment transport. When the near-bed wave orbital motion induced by surface gravity waves is strong enough to mobilize sand grains on the seafloor, nearly symmetrical sand ripples appear due to the redistribution of the mobilized sands. As the flow becomes more intense, the steepness of ripples (defined as the ratio of the ripple height to its length) also increases and vortices are generated. Termed vortex ripples by Bagnold & Taylor (1946), these ripples are characterized by the prominence of spanwise vortices in the overlying flow near the ripple surface, which are periodically formed on the lee-side ripple flank and ejected into the water column from the ripple crest. Field and laboratory studies of vortex ripples show that, for ripples in the orbital regime, the ratio of the wavelength to orbital diameter d_0 is approximately 0.65, and the ratio of the ripple height to wavelength is 0.17 (Longuet-Higgins 1981; Nielsen 1981; Wiberg & Harris 1994; Traykovski *et al.* 1999; O'Donoghue *et al.* 2006; Pedocchi & García 2009; Nelson, Voulgaris & Traykovski 2013; Wang & Yuan 2019). However, the mechanisms that determine these characteristic geometries remain unclear. Understanding the fluid dynamic control and the resulting ripple formation is essential for further explaining the non-equilibrium ripple evolution, ripple migration and transition to various other types of ripples when the flow intensity becomes more energetic (e.g. Traykovski *et al.* 1999). Moreover, ripples influence the bed flow resistance such that accurate prediction of their geometry and evolution is necessary for advancing coastal hydrodynamic models. Through direct numerical simulations (DNSs) of sinusoidal oscillatory flow over out-of-equilibrium vortex ripples, this work focuses on the fluid dynamical controls in the selection of vortex ripple dimensions.

The role of the spanwise vortex in the formation of steep sand ripples was first recognized by Ayrton (1910). Afterward, the close coordination between the ripples and vortices was identified by more comprehensive laboratory experiments. More recently, a fully resolved simulation of sediment transport by Scherer *et al.* (2022) shows that the turbulent coherent structures drive the formation of streamwise-aligned small sand ridges from a completely flat sediment bed without initial perturbation. This study highlights the importance of accurately resolving turbulent coherent structures in the understanding of bedforms. As the oscillatory flow decelerates during each half-cycle, coherent vortices are formed due to the flow separation at ripple crests (Bagnold & Taylor 1946), which drive an intense local accelerating flow close to the ripple surface directed to the ripple crest (van der Werf *et al.* 2007; Yuan & Wang 2019). At this moment, sediment is eroded from the sandy rippled bed and carried by the coherent vortices (Frank-Gilchrist, Penko & Calantoni 2018). These sediment-laden vortices are eventually washed over the ripple crests and ejected into the water column at the opposite side of the ripple during the flow reversal. Meanwhile, sediment trapped within these vortices deposits back to the opposite side of the ripple surface, repairing the erosion that occurred on the previous half-cycle (van der Werf *et al.* 2007; Ribberink *et al.* 2008; Wang & Yuan 2020). The prominent vortex kinematics and the associated sediment transport processes respond rapidly to the disequilibrium in the above coordination, which eventually leads to changes in the ripple morphology. In a study of net sediment transport rate induced by mild bottom slopes, Wang & Yuan (2018) argued that there existed a certain influence zone of the coherent vortices which was important in the selection of ripple wavelength. Through examining the turbulence-averaged flow field of orbital ripples, laboratory experiments (Hare *et al.* 2014; Nienhuis *et al.* 2014; Yuan & Wang 2019) showed that the lee vortices roughly

reached the ripple trough during their generation stage. By visualizing the fluid flow above the sand ripples, Scherer, Melo & Marder (1999) found that the ejected vortices travelled to a location approximately halfway to the adjacent ripple crest.

For short ripples (shorter than the equilibrium wavelength), Hare *et al.* (2014) measured the spatial and temporal flow structure and found that the size of the separation bubble became larger if giving sufficient time for the ripple wavelength to increase. For longer than equilibrium ripples, Andersen, Chabanol & van Hecke (2001) studied the dynamics of sand ripple patterns under oscillatory flow using the standard $k-\epsilon$ turbulence model and indicated that the separation zone did not stretch far enough from the ripple crest such that the ripple trough was not sufficiently eroded. A similar finding was reported by Wang & Yuan (2019) in a full-scale experimental study of the coarse-sand ripples generated by oscillatory flows and a Reynolds-averaged Eulerian two-phase model study (Salimi-Tarazouj *et al.* 2021). In addition to the influence zone concept (Wang & Yuan 2018), the intensity of coherent vortices is also affected by ripple dimensions. In their dynamical models for sand ripples beneath surface waves, Andersen *et al.* (2001) argued that the coherent vortices became weaker for short ripples. This was confirmed by the two-dimensional lattice Boltzmann numerical simulations carried out by Nienhuis *et al.* (2014), which additionally showed that the coherent vortices became stronger for longer ripples. In a full-scale investigation of wave-induced vortex generation events over a movable sediment bed, Nichols & Foster (2007) found that the strength of coherent vortices correlates with the ripple height. The same conclusion was also made by Wang & Yuan (2019).

The bottom shear stress exerted by the seafloor over the overlying flow is considered as another key control in selecting ripple dimensions. This hydrodynamic parameter fundamentally controls a wide range of transport processes in the centimetres-thick bottom boundary layer (Scully *et al.* 2018), such that a lot of sediment transport models for bottom boundary layer flows are formulated using the friction factor to obtain the bottom shear stress, e.g. Madsen (1994), van Rijn (2007), van der A *et al.* (2013) and Wang & Yuan (2020). Using friction factor, predictors (O'Donoghue *et al.* 2006; Pedocchi & García 2009; Nelson *et al.* 2013) for equilibrium ripple dimensions and models (Traykovski 2007; Nelson & Voulgaris 2014, 2015) for predicting the time-dependent evolution of ripples under varying wave conditions are also developed. The role of bottom shear stress in the adjustment of ripple wavelength due to changing wave orbital diameter was confirmed by Traykovski *et al.* (1999) and Traykovski (2007), through field measurements of seafloor ripples under wave-dominated conditions from the LEO15 site and the Martha's Vineyard coastal observatory. In a transient analysis of rippled beds via laboratory experiments, Davis *et al.* (2004) showed that the ripple evolution rate increases with higher normalized bottom stress.

It is generally agreed that the local flow resistance is significantly enhanced by the presence of vortex ripples (Scully *et al.* 2018; Trowbridge & Lentz 2018). Conventionally, the bottom shear stress, defined as the total flow resistance averaged over one ripple wavelength, can be divided into two components: the skin friction and the form drag. The skin friction component is caused by no-slip boundary and fluid viscosity as the flow moves over the ripple surface, while the form drag component is caused by the spatial inhomogeneity in the distribution of pressure on ripple surface, which is directly associated with the near-bed coherent vortices (Yuan & Wang 2019). Usually, the component of form drag is much stronger than the skin friction, such that the fluid dynamical controls of the spanwise coherent vortices and the bottom shear stress are at least partially correlated. This was recently confirmed by the full-scale experimental study conducted by Yuan & Wang

(2018) using an oscillatory water tunnel, where total bottom shear stress was estimated from the change of water pressure for driving the oscillatory flow.

In this study, we present a complete investigation on the fluid dynamical controls of the spanwise coherent vortices, the bottom shear stress on overlying flow and the shear stress on ripple surface through the method of DNS over equilibrium and out-of-equilibrium ripples. As mentioned before, these key physical quantities have been widely used by previous field and laboratory studies to understand ripple geometry. However, these physical quantities are difficult to calculate concurrently and analyse in detail due to the limited measurement resolution or accuracy. Thus, DNS provides an invaluable alternative. Blondeaux, Scandura & Vittori (2004) carried out numerical experiments to investigate the oscillatory flow over a two-dimensional wavy wall with a large amplitude such that the flow separated. Even though the Reynolds number in the simulation was moderate, a three-dimensional turbulent flow was observed where the turbulence dynamics was characterized by the presence of coherent ribs superimposed on the main spanwise vortices. The effects of Reynolds number in turbulent oscillatory flows over moderate-sized vortex ripples were studied by Önder & Yuan (2019) and the detailed flow dynamics over equilibrium rippled bed was analysed. As the main transport agents of turbulent kinetic energy and enstrophy, two classes of coherent columnar vortices are observed: (i) a primary vortex formed at the lee side of the ripple by flow separation at the crest; (ii) a secondary vortex formed beneath the primary vortex by vortex-induced separation. Our work can be considered as a continuation of the recent work by Önder & Yuan (2019) in the application of DNS to study turbulent oscillatory flow over a wavy bottom. A primary objective of our work is to identify the roles of these controls in the selection of equilibrium vortex ripple dimensions by comparing the difference in fluid kinematics resulting from the out-of-equilibrium orbital ripples. Furthermore, we will utilize a comprehensive triple-decomposition flow analysis (Hara & Sullivan 2015) in the present time-dependent and spatially inhomogeneous problem, in order to gain insight into the importance of the ripple-induced fluctuation.

The remainder of this paper is organized as follows. Model formulation, design of numerical experiments and method used for data analysis are presented in § 2. Phase evolution of flow over ripples with different dimensions and shear stress on the ripple surface are shown in § 3. The selection of ripple dimensions is explained through the kinematics carried by the ripple-induced fluctuation in § 4. Finally, conclusions are given in § 5.

2. Problem formulation

2.1. *Flow configuration*

The turbulent oscillatory flow over two-dimensional vortex ripples (illustrated in figure 1) is numerically investigated using DNSs in this study. For the flow configuration, a Cartesian coordinate system is defined on the average plane of the ripple surface, which has a size of $L_1 \times L_2$ in the streamwise and spanwise directions, respectively. In the vertical direction, the physical domain has an average height of L_3, from the average bottom to the top boundary. Driven by a vertically uniform oscillatory pressure gradient, the turbulent flow oscillates periodically in the streamwise direction over vortex ripples characterized by their wavelength of L_r and height of h_r.

For equilibrium vortex ripples, the ripple profile $\eta_r(x_1, x_2)$ is a function of ripple dimensions, i.e. $\eta_r = \eta_r(L_r, h_r)$. As a result, for a specific ripple profile, there are three essential length scales in the present problem: the wave semi-orbital excursion length A,

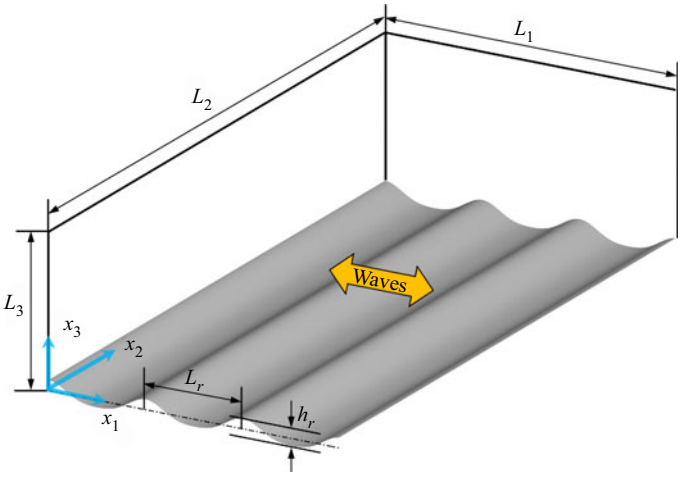

Figure 1. Sketch of the flow domain. Turbulent sinusoidal flow oscillates over a two-dimensional rippled bed with dimensions of L_r and h_r corresponding to the ripple wavelength and height, respectively. The attached Cartesian coordinate system is located on the average bottom with the x_1-axis in the direction of the fluid oscillation, the x_2-axis aligned along the ripple crest and the x_3-axis pointing vertically upwards.

the ripple wavelength L_r and the ripple height h_r. The time scale in this problem is the wave period T_w, where $\Omega_w = 2\pi/T_w$ is the corresponding angular frequency. Based on these characteristic length and time scales, the problem of turbulent oscillatory flow over vortex ripples is characterized by three dimensionless parameters (Önder & Yuan 2019): the Reynolds number

$$Re = \frac{A^2 \Omega_w}{\nu}, \tag{2.1}$$

where ν is the fluid kinematic viscosity; the Keulegan–Carpenter number

$$K_C = 2\pi \frac{A}{L_r}, \tag{2.2}$$

which describes the ratio between the wave semi-orbital excursion and the ripple wavelength; and the ripple steepness

$$s = \frac{h_r}{L_r}. \tag{2.3}$$

For equilibrium orbital ripples, L_r is proportional to A such that K_C is approximately 5. According to field measurements and laboratory experiments, the orbital ripple steepness is approximately 0.17. The Reynolds number is typically in the range of $O(10^4)$ to $O(10^5)$.

The shape of vortex ripples generated by wave boundary layers could be important in the local hydrodynamics and sediment transport, which is a result of many factors such as the oscillatory flow intensity, wave period, wave nonlinearity, horizontal steady streaming, migration direction and sediment properties (Wang & Yuan 2019; Sishah & Vittori 2022). In order to avoid additional complexity, similar to Önder & Yuan (2019), the bottom profile in all our simulations is defined as the superposition of two harmonics, which reads

$$\eta_r = \frac{h_r}{2} \left(\cos k_r x_1 + a \cos 2k_r x_1 \right), \tag{2.4}$$

where $k_r = 2\pi/L_r$ is the wavenumber of the ripple waviness, and the relative amplitude of the second harmonic is prescribed to be $a = 0.17$ following Önder & Yuan (2019).

Therefore, we assume a smooth ripple wall in this study while in a realistic situation the sandy bed is rough with active particle movements, and our ripple profile using superposition of two harmonics is still an idealization of complex ripple geometry observed in nature (Du Toit & Sleath 1981; van der Werf *et al.* 2008).

2.2. *Governing equations*

Although the wave nonlinearity is important in ripple migration and sediment transport (van der Werf *et al.* 2007; Yuan & Wang 2019), we focus on a sinusoidally oscillatory viscous flow over a wavy bottom in order to understand how the leading quantities, namely the ripple wavelength and height, are related to the flow characteristics. Tensor notation is used in this study and the subscript $i = 1, 2, 3$ corresponds to the streamwise, spanwise and vertical directions, respectively. The governing equations are the continuity equation and the incompressible Navier–Stokes equations, which respectively read

$$\frac{\partial u_i}{\partial x_i} = 0, \tag{2.5}$$

$$\frac{\partial u_i}{\partial t} + u_j \frac{\partial u_i}{\partial x_j} = -\frac{1}{\rho}\frac{\partial p}{\partial x_i} + \frac{1}{\rho}\frac{\partial \tau_{ij}}{\partial x_j} + F_w \delta_{i1}, \tag{2.6}$$

where u_i is the velocity field, ρ is the fluid density, p is the pressure field and δ_{ij} is the Kronecker delta; $\tau_{ij} = 2\mu S_{ij}$ is the viscous stress tensor where μ is the fluid dynamic viscosity and S_{ij} is the strain-rate tensor which reads

$$S_{ij} = \frac{1}{2}\left(\frac{\partial u_i}{\partial x_j} + \frac{\partial u_j}{\partial x_i}\right). \tag{2.7}$$

The last term in (2.6) is the driving force in the streamwise direction, where F_w is a vertically uniform oscillatory pressure gradient in the streamwise direction, reading

$$F_w = U_w \Omega_w \sin(\Omega_w t) = U_w \Omega_w \sin\theta. \tag{2.8}$$

The effects of wave skewness (Ribberink & Al-Salem 1994) and asymmetry (Elgar *et al.* 1997) are not considered in this study, and the driven flow has a resultant sinusoidal free-stream velocity $u_w = -U_w \cos\theta$, where U_w is the free-stream velocity amplitude and $\theta = \Omega_w t$ is denoted as the wave phase hereafter. Therefore, corresponding to the wave phase $\theta = 0$, the free-stream velocity starts from the value of $u_w = -U_w$ and decelerates to the instant of flow reversal. Based on (2.8), the wave semi-orbital excursion length is calculated as $A = U_w/\Omega_w$.

In our numerical set-up, the physical domain (figure 1) has a shear-free top boundary where the free-slip, rigid-lid boundary condition is implemented, which reads

$$\frac{\partial u_1}{\partial x_3} = 0, \quad \frac{\partial u_2}{\partial x_3} = 0, \quad u_3 = 0, \quad \text{at } x_3 = L_3. \tag{2.9}$$

In contrast, the bottom of the physical domain is modelled as a fixed bed, and the no-slip boundary condition is applied for the fluid velocities, which is written as

$$u_i = 0, \quad \text{at } x_3 = \eta_r. \tag{2.10}$$

The oscillatory viscous flow over vortex ripples is treated as a boundary layer flow with periodic boundary conditions implemented in the streamwise and spanwise directions.

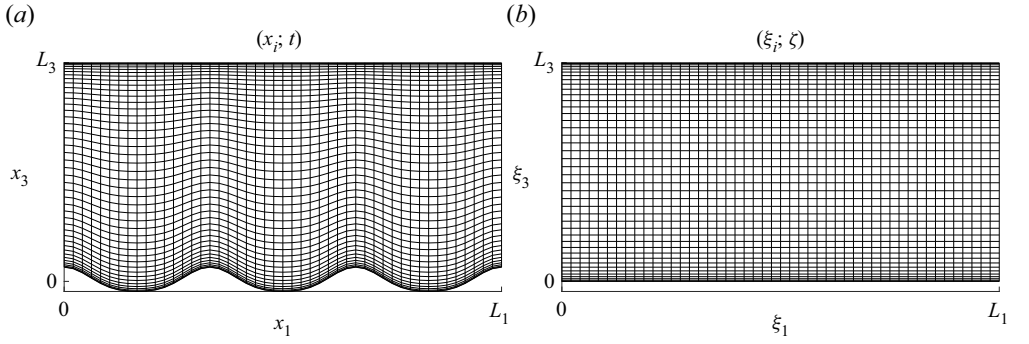

Figure 2. Illustration of the coordinate transformation: (*a*) boundary-fitted grid of the irregular domain in the physical space $(x_i; t)$; (*b*) mapped grid of the rectangular domain in the computational space $(\xi_i; \zeta)$. Note that the uniform grid is applied in both the x_2 and ξ_2 directions.

2.3. *Numerical implementation*

A major difficulty in the simulation of the flow over a bedform is that the physical domain has undulatory boundaries (illustrated in figure 1), which cannot be easily discretized using the commonly used regular grid system. To discretize the irregular physical domain, a boundary-fitted grid system in the Cartesian coordinates $(x_i; t)$ is applied in the physical space, as shown in figure 2(*a*). Then, a new computational coordinate system is introduced by adopting the following algebraic mapping

$$x_1 = \xi_1, \quad x_2 = \xi_2, \quad x_3 = \left(1 - \frac{\eta_r}{L_3}\right)\xi_3 + \eta_r, \quad t = \zeta. \tag{2.11}$$

With this coordinate transformation, the irregular physical domain is transformed into a rectangular computational domain as shown in figure 2(*b*). In the computational space, the top and bottom boundaries are represented by $\xi_3 = L_3$ and $\xi_3 = 0$, respectively. Namely, the resulting size of the computational domain is $L_1 \times L_2 \times L_3$.

By applying the chain rule of partial derivatives, the governing equations (2.5) and (2.6) are rewritten in terms of the curvilinear coordinates $(\xi_i; \zeta)$ in the computational space (Yang & Shen 2010, 2011). The transformed governing equations are integrated in time by the third-order Runge–Kutta scheme. For spatial discretization, we use the pseudo-spectral method on uniform grids ($N_1 \times N_2$) in the ξ_1 and ξ_2 directions, along with the Chebyshev collocation method on the Chebyshev–Gauss–Lobatto points (N_3) in the ξ_3 direction. The open-source code TURBID (https://github.com/yueliangyi/TURBID, Yue, Cheng & Hsu 2019) is upgraded to solve the transformed equations where the numerical schemes are presented in Yue (2020). Figure 3 shows a good agreement of turbulence-averaged quantities between the case kc1.0s1.0 (listed in table 1) and the case C2 in Önder & Yuan (2019). This provides validation of our numerical model.

2.4. *Numerical experiments*

Numerical simulations with a free-stream velocity amplitude of $U_w = 4.42\,\mathrm{cm\,s^{-1}}$ and $T_w = 8.02\,\mathrm{s}$ are carried out in this study. This wave condition results in an angular frequency of $\Omega_w = 0.78\,\mathrm{s^{-1}}$ and a wave semi-orbital excursion of $A = U_w/\Omega_w = 5.65\,\mathrm{cm}$. Four cases (listed in table 1) are designed to study the effect of different ripple dimensions on the resulting fluid kinematics and dynamics, thus revealing the mechanism in the selection of orbital ripple dimensions. In case kc1.0s1.0, the ripple bed is regarded

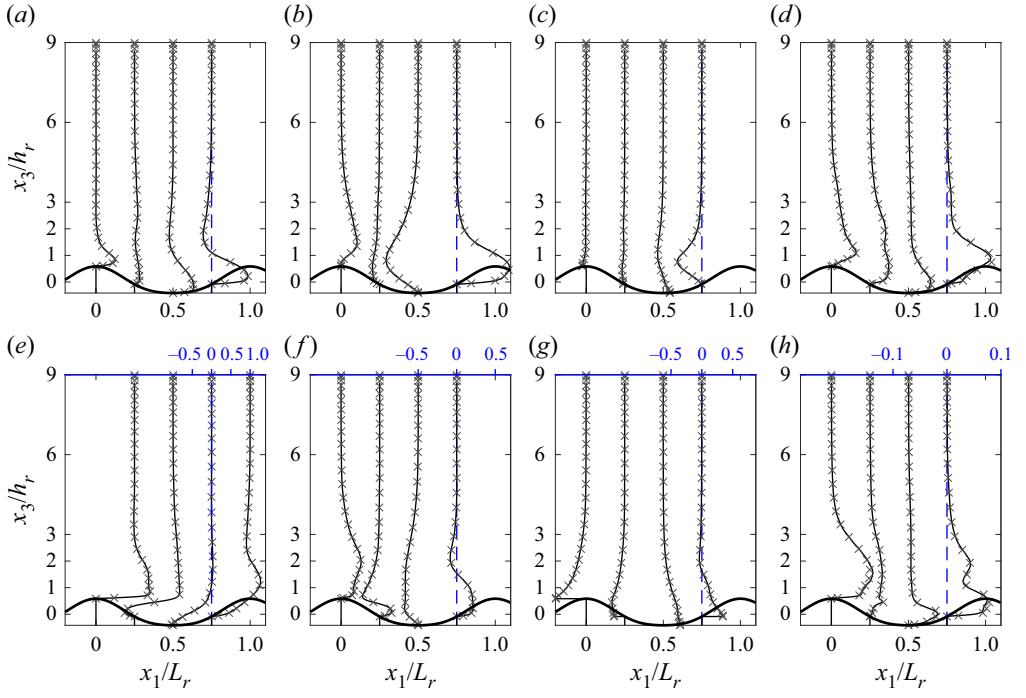

Figure 3. Vertical profiles of the turbulence-averaged streamwise velocity $\langle u_1\rangle_{p2}/U_w$, vertical velocity $\langle u_3\rangle_{p2}/U_w$, pressure $\langle p\rangle_{p2}/\rho U_w$ and turbulence kinetic energy $\langle e_t\rangle_{p2}/U_w^2$ with $e_t = 0.5u_i'u_i'$ at the flow reversal in (*a–d*) and flow peak in (*e–h*). Solid lines correspond to the present simulation results while crosses are results of the case C2 discussed in Önder & Yuan (2019). Variable values are illustrated using a local blue axis, and variable notions are given in § 2.5.

Case	L_r (L_{r0})	h_r (h_{r0})	K_C (K_{C0})	s (s_0)	$L_1 \times L_2 \times L_3$ (L_r)	$N_1 \times N_2 \times N_3$	N_T
kc0.8s1.0	1.25	1.25	0.8	1.0	$3 \times 4.8 \times 1.2$	$324 \times 864 \times 193$	16
kc1.2s1.0	0.83	0.83	1.2	1.0	$3 \times 6 \times 1.8$	$192 \times 576 \times 129$	26
kc1.0s1.0	1.0	1.0	1.0	1.0	$3 \times 6 \times 1.5$	$192 \times 576 \times 129$	26
kc1.0s0.9	1.0	0.9	1.0	0.9	$3 \times 6 \times 1.5$	$192 \times 576 \times 129$	26

Table 1. Physical and computational parameters of the simulations. The reference case kc1.0s1.0 has ripple dimensions of $L_{r0} = 6.78$ cm and $h_{r0} = 1.13$ cm, corresponding to the reference parameters $K_{C0} = 5.24$ and $s_0 = 0.17$. Case names are based on the Keulegan–Carpenter number and the ripple steepness for each run compared with the reference case, such that the case kc0.8s1.0 corresponds to the simulation with $K_C = 0.8K_{C0}$ and $s = 1.0s_0$. The size of the computational domain is selected based on the ripple wavelength of the specific simulation case. Here, N_T is the total run time of simulation in units of wave period.

to be in equilibrium with dimensions of $L_{r0} = 6.78$ cm and $h_{r0} = 1.13$ cm, resulting in the reference parameters of $K_{C0} = 5.24$ and $s_0 = 0.17$. These reference parameters are consistent with most empirical formulas (Pedocchi & García 2009; Nelson *et al.* 2013; Wang & Yuan 2019) for predicting equilibrium vortex ripple dimensions. The other three cases are taken with different ripple dimensions but keep the same K_C or s as the case kc1.0s1.0. By increasing the ripple length by 20 % in case kc0.8s1.0, reducing the ripple length by 20 % in case kc1.2s1.0 or decreasing ripple steepness by 10 % in case kc1.0s0.9,

we can investigate the adequate change in vortex intensity characterizing the turbulent oscillatory flow in an idealized domain. The resulting Reynolds number for all cases is only $Re = 2500$, which is one order smaller than the value in laboratory experiments or field measurements. However, this does not defeat the main objective of this study, which is to reveal the fundamental kinematic characteristics of oscillatory flows over ripples with different dimensions using an idealized model. As shown in table 1, for all four cases, K_C has a range of 4.19 to 6.29, while s has a range of 0.15 to 0.17. Thus, a moderate range of parameters is investigated in this study.

For all numerical simulations presented in this study, the size of the computational domain is chosen based on the ripple wavelength of a specific simulation case. The same criterion is used by Önder & Yuan (2019). The computational domain is confirmed to be large enough by computing the two-point correlation functions. This can also be inferred by the analysis of the computational domain size in appendix B of Önder & Yuan (2019). In all cases, the flow is initialized with appropriate divergence-free sinusoidal perturbations at the flow reversal. Data sampling starts from $t = 6T_w$, when the flow is observed to reach a quasi-steady state, to the end of the simulation ($t = N_T T_w$). The number of grid points for each case simulated in this study is also listed in table 1. The spatial resolutions are assessed in the wall units denoted by a superscript '+', where the grid spacing is non-dimensionalized by the viscous length scale ν/u_τ. The local friction velocity is calculated as $u_\tau = \sqrt{\langle \tau_{w1} \rangle_p / \rho}$, where $\langle \tau_{w1} \rangle_p$ is the streamwise component of the phase-averaged shear stress on the ripple surface (defined in § 3.4). The grid assessment is shown in figure 4, where a grid resolution of $\Delta x_1^+ \leq 13.8$ and $\Delta x_2^+ \leq 9.2$ is found in the streamwise and spanwise directions. In the vertical direction, we obtain $\Delta x_3^+ \leq 0.19$ close to the wall and $\Delta x_3^+ \leq 15.3$ in the middle of the water column. This grid resolution is similar to the one used in Ozdemir, Hsu & Balachandar (2010) for studying the turbulent oscillatory flow over a flat wall. Especially for the case kc0.8s1.0, the grid resolution is even finer due to more intense turbulence.

2.5. *Variable decomposition and notation*

The phase-average approach (Reynolds & Hussain 1972) has been widely used to quantify the modulation of statistical properties of turbulence by the underlying wave motion (Nelson & Fringer 2018; Yue, Cheng & Hsu 2020). The phase averaging of an arbitrary variable ψ in a quasi-steady state is defined as

$$\langle \psi \rangle_p = \frac{1}{N_w} \sum_{n=1}^{N_w} \psi \left(x_1, x_2, x_3; t + nT_w \right), \quad \text{for } 0 \leq t < T_w, \tag{2.12}$$

where the symbol $\langle\ \rangle$ denotes the operation of averaging, and N_w is the number of wave periods during which the averaging is taken. The time averaging of ψ is defined as

$$\bar{\psi} = \frac{1}{N_w T_w} \int_0^{N_w T_w} \psi \left(x_1, x_2, x_3; t \right) \, \mathrm{d}t. \tag{2.13}$$

Note that $t = \zeta$ in the coordinate transformation (2.11), such that the defined time and phase averaging is also applicable in the transformed domain, i.e. figure 2(*b*). In addition

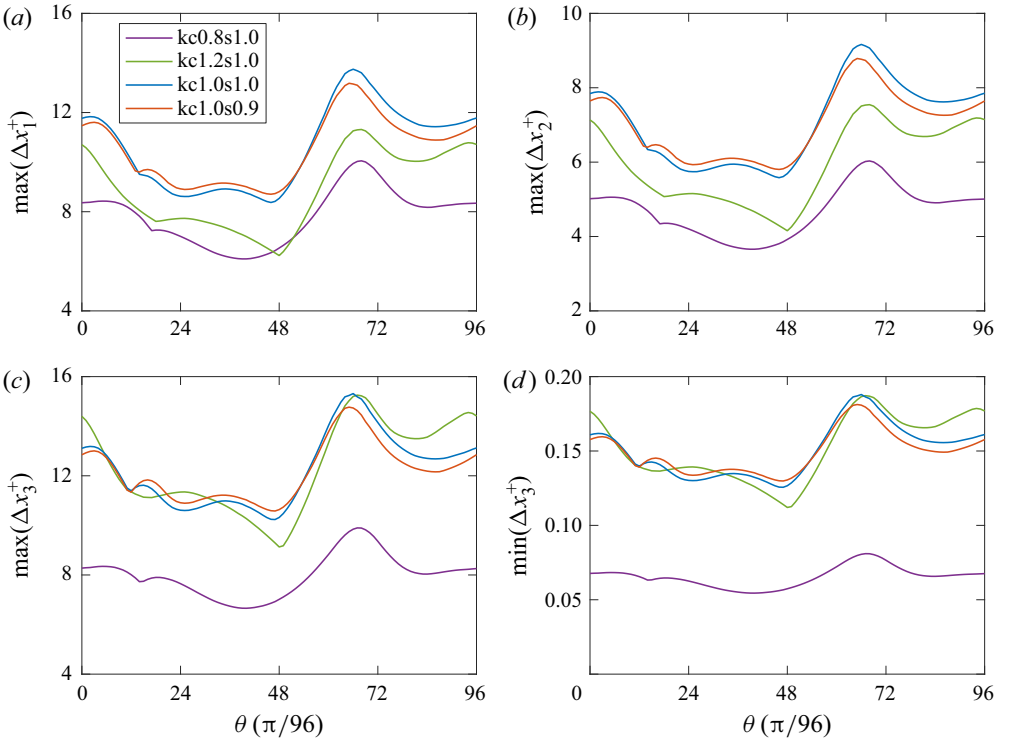

Figure 4. Grid resolution in wall units over a half-flow cycle: (*a*,*b*) maximum grid spacings in the streamwise and spanwise directions, respectively; (*c*) maximum and (*d*) minimum grid spacings in the vertical direction.

to the averaging over time, spatial averaging in the transformed domain reads

$$\langle \psi \rangle_i = \frac{1}{L_i} \int_0^{L_i} \psi\left(\xi_1, \xi_2, \xi_3; \zeta\right) \mathrm{d}\xi_i, \tag{2.14}$$

where the subscript i ($i = 1$, 2 or 3) of the average operator $\langle\ \rangle$ denotes a spatial averaging in the corresponding direction.

In this study, the bedform is two-dimensional and the flow is regarded to be homogeneous in the spanwise direction. Consequently, the turbulence-averaging operator $\langle\ \rangle_{p2}$, implying the phase and ξ_2 averaging, is used to separate the turbulence fluctuation. With the defined turbulence averaging, the variable ψ is decomposed as $\psi = \langle\psi\rangle_{p2} + \psi'$, where ψ' is the corresponding turbulent fluctuation component. Furthermore, for the statistically steady turbulent flow over a bedform, the turbulence-averaged quantity can be further decomposed using a spatial (streamwise) averaging (Hara & Sullivan 2015), leading to a triple decomposition of the variable ψ as

$$\psi = \langle\psi\rangle_w\left(\xi_3; \zeta\right) + \langle\psi\rangle_r\left(\xi_1, \xi_3; \zeta\right) + \psi'\left(\xi_1, \xi_2, \xi_3; \zeta\right), \tag{2.15}$$

where $\langle\psi\rangle_{p2} = \langle\psi\rangle_w + \langle\psi\rangle_r$. The term $\langle\psi\rangle_w = \langle\psi\rangle_{p12}$ is the ripple-averaged but time-dependent mean flow. Due to its time dependency under wave motion, it is called the ripple-averaged wave-induced motion in this study. Accordingly, the term $\langle\psi\rangle_r = \langle\psi\rangle_{p2} - \langle\psi\rangle_w$ is denoted as the ripple-induced fluctuation. Note that, the phase-, time- and spatial-average operations correspondingly defined in (2.12) to (2.14) are commutative. The triple decomposition defined in (2.15) is applied to the instantaneous velocity

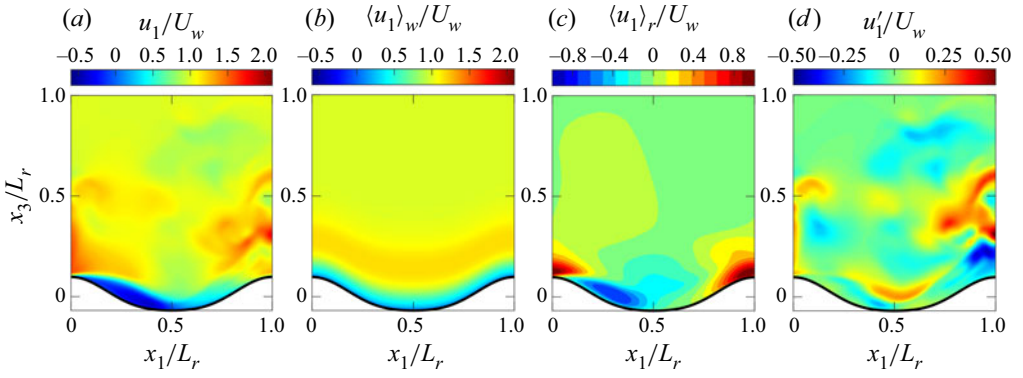

Figure 5. Illustration of the triple decomposition of the streamwise velocity: (*a*) instantaneous velocity profile u_1 at a flow peak; (*b*) the ripple-averaged wave-induced motion $\langle u_1\rangle_w$; (*c*) the ripple-induced fluctuation $\langle u_1\rangle_r$; (*d*) the turbulent fluctuation u_1'. All the velocities are normalized by the free-stream velocity amplitude U_w.

profile u_1 at flow peak (crest) in the oscillatory flow (see figure 5). The component of ripple-averaged wave-induced motion contains the background velocity with a relatively uniform distribution far from the rippled bed (figure 5*b*). Organized spatial variation in the velocity field u_1 (e.g. vortices) is contained in the ripple-induced fluctuation, which has higher intensity close to the ripple surface (figure 5*c*). The random flow structure is found in the turbulent fluctuation (figure 5*d*). Similar triple decomposition approaches have been widely used in previous works (Sullivan, Mcwilliams & Moeng 2000; Yang & Shen 2010; Buckley & Veron 2019; Zhang, Huang & Xu 2019).

3. Ripple dimensions and fluid kinematics

Commonly observed in the coastal ocean, vortex ripples are generated in wave-exposed bottom boundary layers caused by the interaction between the overlying flow and the sandy seabed (van der Werf *et al.* 2007; Nayak *et al.* 2015), resulting in a shear stress on the ripple surface. This shear stress, on one hand, drives sediment transport and controls ripple geometry. On the other hand, the shear stress is experienced by the overlying flow and leads to energy dissipation by the skin friction and form drag. During the interaction, the dynamics of the overlying flow is dominated by the generation and subsequent ejection of coherent vortices on ripple flanks (Nichols & Foster 2007, 2009; van der Werf *et al.* 2007; Yuan & Wang 2019). All these features will be examined in this section.

3.1. *Vortex evolution in turbulence-averaged flow*

The kinematics of turbulence-averaged flow over ripples are presented in this section, with a special emphasis on the motion of spanwise coherent vortices. To this end, the spanwise vorticity is calculated from the turbulence-averaged velocities as

$$\langle\omega_2\rangle_{p2} = \frac{\partial\langle u_3\rangle_{p2}}{\partial x_1} - \frac{\partial\langle u_1\rangle_{p2}}{\partial x_3}. \tag{3.1}$$

However, the criterion of vorticity cannot always give a satisfactory identification of the region with strong swirling motions if the ambient shear is also strong. For clear identification of vortices, an improved vortex identification method is needed. Alternatively, defined as a measure of local twisting rate within a vortex, the swirling

strength criterion proposed by Zhou *et al.* (1999) has been widely used in measured flow fields over rippled beds (Nichols & Foster 2007; Rodríguez-Abudo & Foster 2014; Yuan & Wang 2019). Although the method of swirling strength can better identify vortices compared with the vorticity, the criterion is still prone to severe contamination by the strong background shearing (Gao & Liu 2018), which is universal in a bottom boundary layer flow. In this study, we adopt a new vortex identification method using the vortex vector (Tian *et al.* 2018, 2020) to differentiate the vortices from the background shear flow. The vortex vector is defined based on the local rotation of fluid elements, thus it can exclude the ambient shearing contamination and accurately quantify the local rotational strength. A vortex vector at a point is a vector quantity representing the local fluid rotation and it is defined as

$$\boldsymbol{R} = 2\omega_{rot}\boldsymbol{r}, \tag{3.2}$$

where $\boldsymbol{r}$ is the normalized direction of the local fluid-rotation axis which is calculated as the unit eigenvector corresponding to the real eigenvalue of the velocity gradient tensor $\partial u_i/\partial x_j$, and ω_{rot} is the local fluid-rotational angular velocity, which reads

$$\omega_{rot} = \begin{cases} \beta - \alpha, & \text{if } \beta > 0 \text{ and } \alpha^2 < \beta^2, \\ \beta + \alpha, & \text{if } \beta < 0 \text{ and } \alpha^2 < \beta^2, \\ 0, & \text{if } \alpha^2 \geq \beta^2. \end{cases} \tag{3.3}$$

In (3.3), the parameters α and β, defined as

$$\alpha = \frac{1}{2}\sqrt{\left(\frac{\partial V_2}{\partial X_2} - \frac{\partial V_1}{\partial X_1}\right)^2 + \left(\frac{\partial V_2}{\partial X_1} + \frac{\partial V_1}{\partial X_2}\right)^2}, \tag{3.4}$$

$$\beta = \frac{1}{2}\left(\frac{\partial V_2}{\partial X_1} - \frac{\partial V_1}{\partial X_2}\right), \tag{3.5}$$

are calculated from the velocity vector $\boldsymbol{V}$ defined in a local reference frame $\boldsymbol{X}$, where the X_3-axis is parallel to $\boldsymbol{r}$, $\partial V_1/\partial X_3 = 0$ and $\partial V_2/\partial X_3 = 0$. Based on (3.2) to (3.5), a vortex is then defined as a connected region where $\boldsymbol{R} \neq \boldsymbol{0}$, and the iso-surface of the magnitude of vortex vector $|\boldsymbol{R}|$ (denoted as the vortex strength hereafter) can distinctly represent the core of a vortex (Tian *et al.* 2018).

Evolution of the turbulence-averaged velocity and the spanwise vorticity fields throughout the first half-cycle of a wave period is illustrated in figure 6, from the wave phase just after the maximum negative free-stream velocity (*a*) $\theta = 16\pi/96$ to the wave phase at the maximum positive free-stream velocity (*f*) $\theta = 96\pi/96$. For a better presentation, a local ripple coordinate $\check{x}_1 = x_1 - x_{1c}$ is employed with x_{1c} being the streamwise location of a ripple crest, such that the ripple crest is always located at $\check{x}_1 = 0$ and the sign of $\check{x}$ differentiates the two ripple flanks. Due to the periodicity of results in the streamwise direction, the field of view is presented as one ripple wavelength. Although the four cases shown in figure 6 have very different ripple dimensions (see table 1), most of the interesting fluid kinematics happen close to the ripple surface, and we focus on a region from the ripple trough to the specific height of $4h_{r0}$ in the vertical direction.

In each plot of figure 6, the turbulence-averaged velocities ($\langle u_1\rangle_{p2}$, $\langle u_3\rangle_{p2}$) are presented by a vector field. Shown as the grey arrows, the evolution of the ambient flow is identified in a region far from the ripple bed, while the modulation of flow caused by the coherent vortices can be clearly observed in a region close to the rippled bed with a notable enhancement in the velocity magnitude. Using the turbulence-averaged velocity field, the

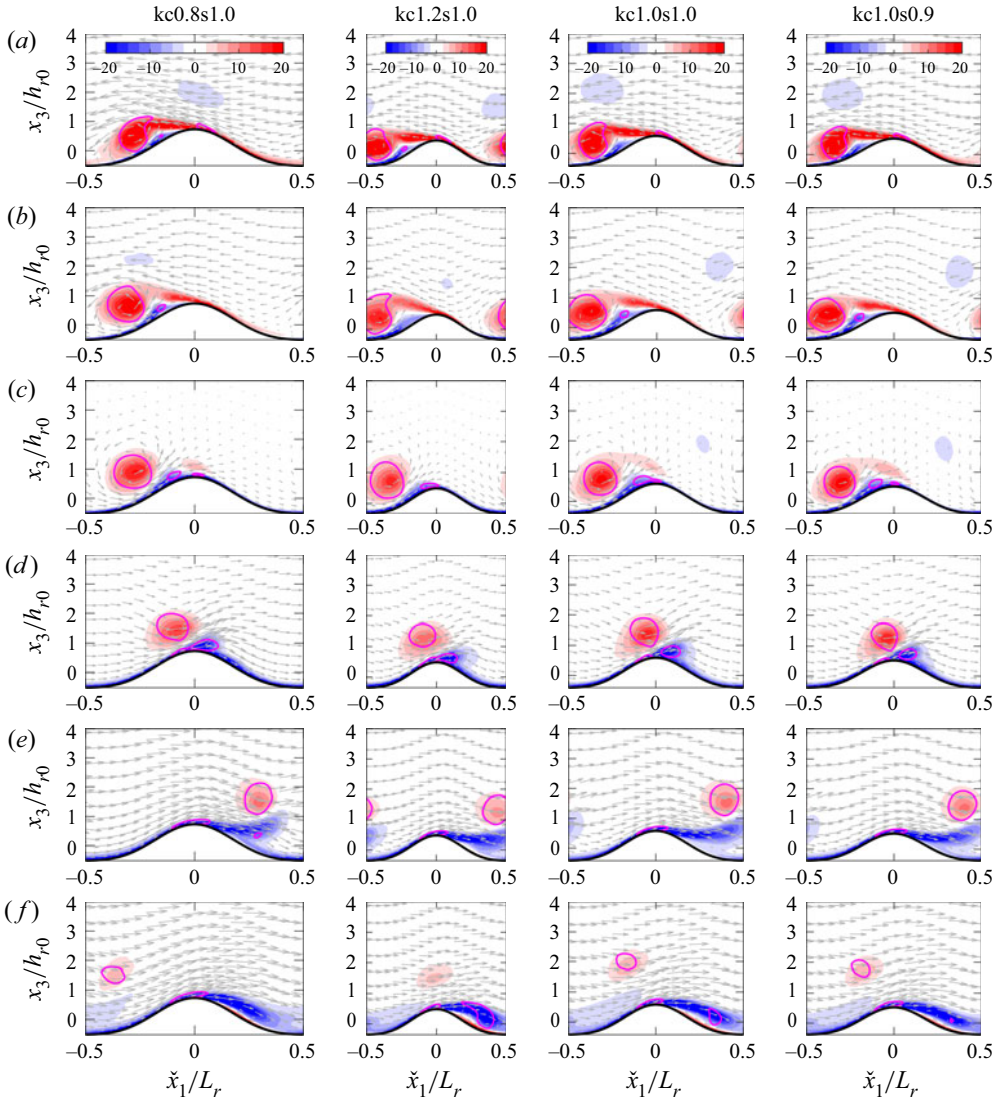

Figure 6. Evolution of the turbulence-averaged velocity and the spanwise vorticity fields throughout the half-cycle of a wave period, from the wave phase (*a*) $\theta = 16\pi/96$ to (*f*) $\theta = 96\pi/96$. The normalized turbulence-averaged velocities $(\langle u_1\rangle_{p2}, \langle u_3\rangle_{p2})/U_w$ are presented as a vector field denoted by the grey arrows, while the corresponding normalized spanwise vorticity $\langle\omega_2\rangle_{p2}/(U_w/L_{r0})$ is presented as iso-surfaces. The coherent vortices are identified using the vortex vector method as the purple contour lines, where the normalized vortex strength criterion of $\langle|\boldsymbol{R}|\rangle_{p2}/(U_w/L_{r0}) = 3$ is implemented. A local ripple coordinate $\check{x}_1 = x_1 - x_{1c}$ is employed with x_{1c} being the streamwise location of a ripple crest.

corresponding spanwise vorticity $\langle\omega_2\rangle_{p2}$ is calculated following the (3.1) and presented as the iso-surfaces in figure 6. Illustrated by the change of colours of the vorticity iso-surfaces for each simulation, vortices form at the previous accelerating phase before the flow reversal (when $\theta = 0$) continues to absorb the flow energy in the deceleration phase between $0 < \theta \leq \pi/2$ (figure 6*a–c*). During this stage, a primary vortex in the lee ripple flank with $\check{x}_1 < 0$ can be clearly identified as a closed region with a high positive spanwise vorticity. In the acceleration stage in the interval $\pi/2 < \theta \leq \pi$ (figure 6*d–f*),

the coherent vortices separate from the ripple crest, travel large distances with their self-induced velocities, and produce positive jet-like flows as they pass the ripple crest. Meanwhile, the strength of the spanwise (positive) vorticity owned by the ejected primary vortex drops continually to nearly zero. The primary vortex eventually disappears due to the viscous effects. Therefore, the deceleration and acceleration phases are respectively denoted as the vortex-formation and jet-ejection stages in Önder & Yuan (2019).

In addition to the high spanwise vorticity, the coherent vortices are identified using the vortex vector method. For each wave phase, the vortex strength field $\langle|\boldsymbol{R}|\rangle_{p2}$ is calculated from the corresponding turbulence-averaged flow. The normalized vortex strength criterion of $\langle|\boldsymbol{R}|\rangle_{p2}/(U_w/L_{r0}) = 3$ has been used, which are plotted as the purple contour lines in figure 6. With the threshold of vortex strength used here, vortices are nicely outlined as circles or ellipses over the ripple bed. At most wave phases, more than one vortex has been clearly detected among which there is a primary vortex usually associated with strong spanwise vorticity. In addition to the primary vortex, a secondary or even tertiary vortex around the primary one and near the ripple surface is also detected. The evolution of primary vortices is identified by the size of these iso-lines through different wave phases. For each simulation, during the vortex-formation stage (figure 6*a–c*), the area circled by the iso-line is growing and hence the newly born primary vortex is developing into larger size and absorbing more energy. During the wave phases (figure 6*d–e*) when the ejection of the primary vortex is observed, there is no noticeable change in the primary vortex size, and in fact, the turbulence-averaged spanwise vorticity in the primary vortex starts to decay. In the late stage of jet-ejection (figure 6*e–f*), similar to the spanwise vorticity, the primary vortex size and the intensity are diminishing until its disappearance.

The significance of flow velocity associated with the ripple-induced fluctuation ($\langle u_i\rangle_r$, see definition in (2.15)) is also investigated. Similar to the turbulence-averaged spanwise vorticity defined in (3.1), the vorticity carried by the ripple-induced velocity fluctuation is calculated as

$$\langle\omega_2\rangle_r = \frac{\partial\langle u_3\rangle_r}{\partial x_1} - \frac{\partial\langle u_1\rangle_r}{\partial x_3}. \tag{3.6}$$

Evolution of the ripple-induced velocity fluctuation and the corresponding spanwise vorticity fields throughout the first half-cycle of a wave period is shown in figure 7. It is straightforward to find that large velocities are associated with strong vorticity $\langle\omega_2\rangle_r$ in figure 7. Compared with the turbulence-averaged velocities in figure 6, there is no phase-dependent background velocity field in the ripple-induced fluctuation. Same as before, coherent vortices can be clearly identified in the ripple-induced fluctuation velocity using the normalized vortex strength with a criterion of $\langle|\boldsymbol{R}|\rangle_{p2}/(U_w/L_{r0}) = 3$. To facilitate the comparison, the coherent vortices detected from the velocity field of turbulence-averaged flow and that of ripple-induced fluctuation are both shown as the purple and green iso-lines in figure 7, respectively. From the close overlapping between these iso-lines, it is clear that the ripple-induced fluctuation carries almost entirely these coherent vortices and the ripple-averaged wave-induced motion is of negligible importance.

One of the significant results that distinguishes the coherent vortices over different ripple dimensions is their different strengths (studied in § 3.2) and trajectories. In figure 6, the difference in trajectories of the primary vortices are evident and for comparison, the results are shown here by normalizing the horizontal trajectory with respect to the individual ripple wavelength of each case. In case kc0.8s1.0 where the ripple wavelength is larger than the equilibrium ripple case kc1.0s1.0, the primary vortex first formed at a location relatively close to the ripple crest during the vortex-formation stage (see $\theta = 16\pi/96$

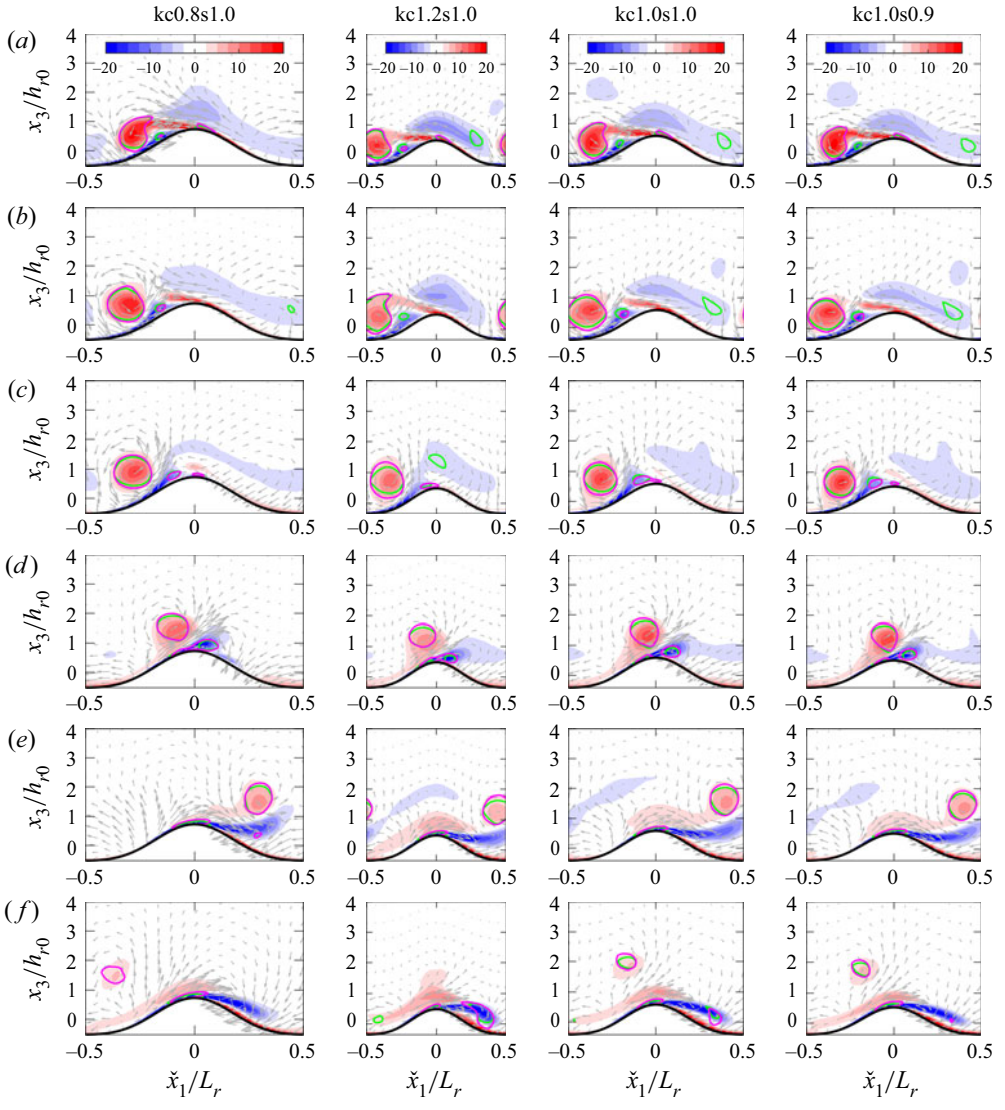

Figure 7. Evolution of the turbulence-averaged velocity and spanwise vorticity fields in the ripple-induced fluctuation throughout the half-cycle of a wave period, from the wave phase (*a*) $\theta = 16\pi/96$ to (*f*) $\theta = 96\pi/96$. The normalized turbulence-averaged velocities $(\langle u_1\rangle_r, \langle u_3\rangle_r)/U_w$ are presented as a vector field denoted by the grey arrows, while the corresponding normalized spanwise vorticity $\langle\omega_2\rangle_r/(U_w/L_{r0})$ is presented as the iso-surface. The coherent vortices are identified in the turbulence-averaged flow and the ripple-induced fluctuation with the criterion of normalized vortex strength $\langle|\boldsymbol{R}|\rangle_{p2}/(U_w/L_{r0}) = 3$, which are respectively shown as the purple and green iso-lines. The local ripple coordinate $\check{x}_1$ is employed.

shown in figure 6*c*); the vortex centre is located at $\check{x}_1/L_r = -0.25$ for kc0.8s1.0 comparing with $\check{x}_1/L_r = -0.35$ for kc1.0s1.0). Interestingly, the formed lee primary vortex in case kc0.8s1.0 also cannot travel as far away downstream as the equilibrium ripple case kc1.0s1.0 during the jet-ejection stage (see figure 6(*e*), the vortex centre is located at $\check{x}_1/L_r = 0.3$ for kc0.8s1.0 comparing with $\check{x}_1/L_r = 0.4$ for kc1.0s1.0). The exact opposite in vortex trajectory can be observed in case kc1.2s1.0 where the ripple wavelength is shorter than the equilibrium value. A similar finding is reported in an experiment by

increasing the orbital excursion length (Hare *et al.* 2014). By reducing the ripple height, the centre of the primary vortex during its formation shifts towards the ripple crest slightly (see figure 6*b*). After the ejection of primary vortex from the ripple crest, figure 6 also shows that the small reduction of ripple height does not affect notably on how much distance a primary vortex can travel.

Motivated by these observations, the trajectory of the primary vortex is quantified by its weighted centre (x_{w1}, x_{w3}), which is defined as

$$x_{wi} = \frac{\displaystyle\int_0^{L_r}\int_{\eta_r}^{L_3} w x_i \,\mathrm{d}x_1\,\mathrm{d}x_3}{\displaystyle\int_0^{L_r}\int_{\eta_r}^{L_3} w \,\mathrm{d}x_1\,\mathrm{d}x_3}, \tag{3.7}$$

where the subscript $i = 1$ or 3. The weight function $w = \langle|\boldsymbol{R}|\rangle_{p2}$, when a position is found to be inside or on the primary vortex. Otherwise, w is set to zero. Using the weighted centre, trajectories of the primary vortex for the four cases are presented in both the physical (figure 8*a*) and transformed (figure 8*b*) domains. Since the case kc0.8s1.0 has the largest ripple height as $h_r = 1.25h_{r0}$, the primary vortex travels along a higher trajectory in the physical domain. However, this feature disappears in the transformed domain. Figure 8(*b*) shows that the parameter K_C does not affect the trajectory of primary vortex evidently in regard to its height for the early and intermediate stages of the vortex evolution. It is only approaching the late stage of vortex evolution that the primary vortex in case kc1.0s1.0 shows the highest trajectory. On the contrary, both in the physical and transformed domain, the height of the primary vortex trajectory shows a clear dependence on the ripple steepness parameter s. For the case kc1.0s0.9 with a smaller ripple steepness, the trajectory is closer to the ripple surface. The distance a primary vortex can travel in the streamwise direction during the vortex-formation stage is also observed in figure 8. Generally, the primary vortex can travel relatively farther downstream towards the ripple trough and beyond (where $x_1/L_r < 1$) for K_C greater than K_{C0} and its dependence on the ripple steepness is weak. Circles in figure 8 correspond to the first peak in the form drag bottom shear stress shown in figure 11(*c*), which will be discussed later. Beyond these marked normalized positions, the primary vortices are about to be ejected from the ripple crest into the water column (figure 12*c*,*d*). During the vortex-ejection stage, the trajectories in the transformed domain are elevated even though they look flat in the physical domain (figure 8*a*). Overall, from its generation to full dissipation, the primary vortex is close to the rippled bed in a region below $x_3 = 4h_{r0}$ (see figure 6). This confirms our finding from figure 6.

3.2. *Time-averaged vortex influence zone*

Illustrated in §§ 3.1, a coherent vortex in the turbulence-averaged field dominates the near-bed kinematics of overlying flow. After time averaging, the result of columnar coherent vortices in the carrying flow is illustrated by time-averaged circulation and the corresponding spanwise vorticity (see figure 9). In the figure, the time-averaged velocities $(\langle\overline{u_1}\rangle_2, \langle\overline{u_3}\rangle_2)$ are presented as a vector field and denoted as the grey arrows. Two counter-rotating mean circulations are observed, where the time-averaged spanwise vorticity $\langle\overline{\omega_2}\rangle_2$, presented as iso-surfaces, has the opposite direction (see red and blue colours). The two circulations are respectively located above the two ripple flanks, centred at the same height with respect to the ripple crest due to the present simple harmonic flow and symmetric ripple profile. They produce a strong mean velocity close to the ripple

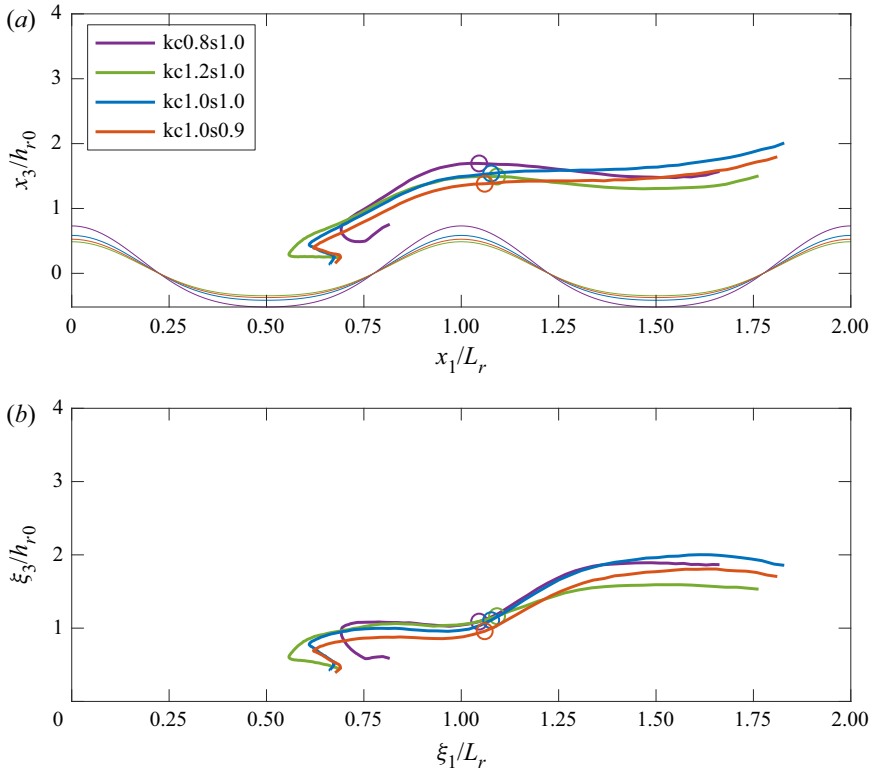

Figure 8. Weighted centre trajectories of primary vortex during the first half-wave cycle: (*a*) trajectories in the physical domain denoted as thick solid lines; (*b*) trajectories in the transformed domain. Thin lines in (*a*) are the ripple profiles for the four numerical cases. Vertical and horizontal coordinates are respectively normalized by h_{r0} and L_r for a better comparison. Circles correspond to the group ① in figure 11(*c*), which locates the normalized position of vortex ejection into the water column. Results of one ripple are presented for illustration.

surface, which conveys water toward the ripple crest. If sediment particles were present, this flow pattern would drive particle fluxes toward the ripple crest and hence maintains the ripple shape. Thus, the two circulations are highly related to the formation mechanism of vortex ripples (Charru, Andreotti & Claudin 2013). Due to the symmetry of oscillatory flow and ripple profile, the two circulations are equal in strength. A similar observation was obtained in laboratory experiments by, for example, Yuan & Wang (2019) and they further demonstrate that if the symmetry is altered, the flow pattern and ripple profile must adjust toward another equilibrium and possibly migrate. Specifically, when the size of circulation zone is smaller than the distance between the adjacent ripples, the circulation can erode the ripple flank and drive the splitting of ripples. On the contrary, when the size of the circulation zone is too large, the vortices tend to carry more particles from the ripple crest and deposit them toward the trough and cause the merging of ripples (Salimi-Tarazouj *et al.* 2021). Therefore, it is of fundamental importance to relate the circulation pattern to ripple dimensions.

The strength of these two circulations is quantified by a flux of vorticity, which is defined as the integral of the spanwise vorticity magnitude through the x_1–x_3 section of

Case	kc0.8s1.0	kc1.2s1.0	kc1.0s1.0	kc1.0s0.9
Γ_2 ($U_w L_{r0}$)	0.9389	0.6143	0.8054	0.7483
Γ_v ($U_w L_{r0}$)	0.2457	0.2037	0.2461	0.2228
f_τ ($\rho U_w^2 L_{r0}$)	0.0364	0.0269	0.0278	0.0236
L_c (L_{r0})	0.7185	0.6514	0.7144	0.6853

Table 2. Indices resulting from fluid dynamical controls without spatial averaging over one ripple wavelength.

the physical domain, written as

$$\Gamma_2 = \int_0^{L_r} \int_{\eta_r}^{L_3} \langle |\overline{\omega_2}| \rangle_2 \, \mathrm{d}x_1 \, \mathrm{d}x_3. \tag{3.8}$$

Table 2 presents the computed Γ_2 for the four cases investigated here where $\Gamma_2 = 0.9389$ $U_w L_{r0}$ in case kc0.8s1.0 is found to be the largest. This indicates that the case kc0.8s1.0 has a relatively strong time-averaged circulation, illustrated by the relatively large velocity around the ripple crests in figure 9(*a*). The case kc1.2s1.0 has the smallest strength of circulation as $\Gamma_2 = 0.6143$ $U_w L_{r0}$ which could be significantly suppressed by the short ripple wavelength (figure 9*b*). As the case kc0.8s1.0 has the largest ripple wavelength (the smallest value of K_C) and thus the longest integration length in (3.8), it is more reasonable to quantify the circulation strength with non-dimensional values. When Γ_2 is normalized by the corresponding ripple wavelength L_r for each case, indicating the strength of circulation per unit area (see table 3), it is clear that the case kc1.0s1.0 has the strongest normalized circulation of 0.8054 U_w. The analysis shown here suggests that variation in ripple wavelength away from the equilibrium value reduces the strength of time-averaged normalized circulations. In other words, the equilibrium ripple wavelength corresponds to the maximum of time-averaged normalized circulation. Another important finding from figure 9 is that each of the four cases has different time-averaged influence regions. Indicated by the area occupied by the strong time-averaged spanwise vorticity, there are two influence regions for each ripple crest just above the left and right ripple flanks. In case kc0.8s1.0, when compared with case kc1.0s1.0, the influence regions between two ripple crests are relatively further apart, while they are closer in case kc1.2s1.0. Reducing ripple height also slightly increases the distance between the influence regions (figure 9*d*) while reducing the strength of circulation compared with the equilibrium case (see tables 2 and 3).

The idea of a vortex influence zone is similar to the influence region defined based on the time-averaged spanwise vorticity, which is introduced by Wang & Yuan (2018) to explain the asymmetry in ripple profiles caused by gently sloping bottoms. To better quantify the vortex influence zone, we take the strength of the time-averaged vortex vector field $\langle |\bar{\boldsymbol{R}}| \rangle_2$ as the key parameter, which is shown in figure 10. The purple iso-lines shown in figure 9 correspond to the criterion $\langle |\bar{\boldsymbol{R}}| \rangle_2 / (U_w / L_{r0}) = 1.5$. Intuitively, both figure 9 and figure 10 illustrate the influence region caused by the evolution of coherent vortices. Comparing these two figures, the strong time-averaged spanwise vorticity is roughly located inside the iso-lines of $\langle |\bar{\boldsymbol{R}}| \rangle_2 / (U_w / L_{r0}) = 1.5$. However, the field $\langle |\bar{\boldsymbol{R}}| \rangle_2$ concentrates in a region over the ripple trough, from which the boundary of vortex influence can be more clearly differentiated. Following (3.7), locations of the weighted centre of the iso-lines are also calculated. Based on these weighted centres, the distance between two adjacent centres around one ripple crest is defined as L_c and illustrated in figure 10(*a*), which measures

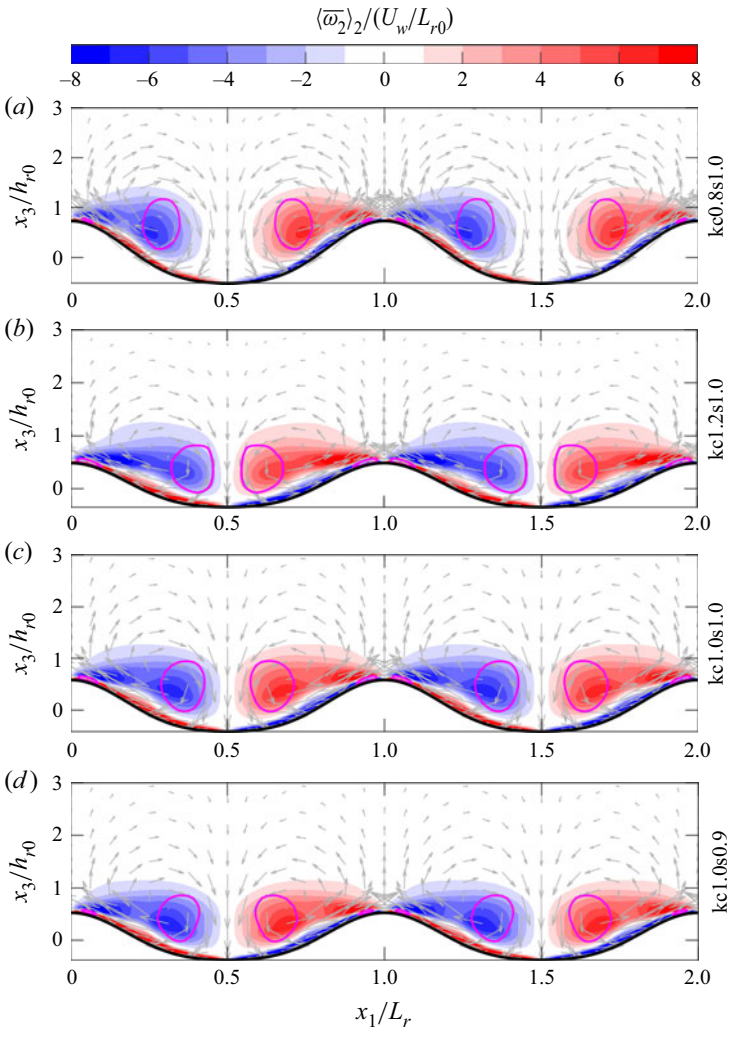

Figure 9. Time- and ξ_2-averaged velocity and vorticity fields. The normalized time-averaged velocities $(\langle\overline{u_1}\rangle_2, \langle\overline{u_3}\rangle_2)/U_w$ are presented as a vector field denoted by the grey arrows, while the corresponding normalized spanwise vorticity $\langle\overline{\omega_2}\rangle_2/(U_w/L_{r0})$ is presented as iso-surfaces. Purple contour lines denote the normalized strength of the time-averaged vortex vector field (shown in figure 10) where the criterion $|\langle\bar{\boldsymbol{R}}\rangle_2|/(U_w/L_{r0}) = 1.5$ is implemented. Results of two ripples are presented for illustration.

the width of the coherent vortex influence zone (see table 2). In case kc1.0s1.0, where the ripple dimensions are in equilibrium, the distance $L_c = 0.7144\ L_{r0}$. When increasing the ripple wavelength by 25 % while keeping the same ripple steepness in case kc0.8s1.0, we observe $L_c = 0.7185\ L_{r0}$ and the increase in L_c is negligible even though the coherent vortex has more space to evolve. This means that there exists a maximum width of influence zone for a specific ripple steepness (compare with $L_r = 0.6853\ L_{r0}$ for case kc1.0S0.9). Interestingly, a notably smaller value of $L_c = 0.6514\ L_{r0}$ is observed in case kc1.2s1.0 with a reduced ripple wavelength, where the primary vortex that was shed from the ripple crest can reach a location beyond the ripple trough towards the adjacent ripple crest (figures 6*b* and 8). This leads to cancellation in the time-averaged vortex vector field and is presented as a 'confliction' in the field of $\langle|\bar{\boldsymbol{R}}|\rangle_2$, which can lead to

Case	kc0.8s1.0	kc1.2s1.0	kc1.0s1.0	kc1.0s0.9
Γ_2/L_r (U_w)	0.7511	0.7371	0.8054	0.7483
Γ_v/L_r (U_w)	0.1966	0.2444	0.2461	0.2228
f_τ/L_r (ρU_w^2)	0.0291	0.0323	0.0278	0.0236
$\overline{\lvert\langle\tau_t\rangle_w\rvert}$ (ρU_w^2)	0.0401	0.0401	0.0383	0.0327
L_c/L_r	0.5748	0.7817	0.7144	0.6853

Table 3. Indices resulting from fluid dynamical controls after spatial averaging over one ripple wavelength.

merging of ripples, as mentioned earlier. As mentioned before, by reducing the ripple height in case kc1.0s0.9, a smaller value of $L_c = 0.6853\ L_{r0}$ is found, meaning that the ripple height limits how far the vortex separation can reach. Consequently, smaller ripple steepness results in small ripple length as seen in the sub-orbital ripples (Wiberg & Harris 1994; Pedocchi & García 2009). The corresponding normalized distance L_c/L_r is listed in table 3, where the value of $L_c/L_r = 0.7817$ in case kc1.2s1.0 is recognized to be the largest, indicating a possible strong interference in the flow over two neighbour ripples.

In addition to the vorticity flux defined in (3.8) based on the time-averaged spanwise vorticity, we further calculate the vortex strength flux using $\langle\lvert\overline{\boldsymbol{R}}\rvert\rangle_2$ since it is effective in quantifying the averaged strength of vortices generated over the ripples. Defined as the integration of time-averaged vortex strength, the vortex strength flux is written as

$$\Gamma_v = \int_0^{L_r} \int_{\eta_r}^{L_3} \langle\lvert\overline{\boldsymbol{R}}\rvert\rangle_2 \,\mathrm{d}x_1\,\mathrm{d}x_3. \tag{3.9}$$

Listed in table 2, the case kc1.0s1.0 is found to have the maximum vortex strength flux as $\Gamma_v = 0.2461\ U_w L_{r0}$ among the four cases investigated. Even after averaging over one ripple wavelength, the vortex strength flux per ripple wavelength (listed in table 2) in case kc1.0s1.0 remains the largest. Simulation results clearly show that the equilibrium ripple wavelength exists to cause the strongest vortex motion driven by oscillating overlying fluid. Through the comparison between cases with the same ripple wavelength (kc1.0s1.0 and kc1.0s0.9), results also confirm that the larger ripple height results in stronger vortex motion. This finding also supports the conclusion reported by the field measurement (Nichols & Foster 2007). Note that the Keulegan–Carpenter number in Nichols & Foster (2007) is defined based on the ripple height rather than the ripple wavelength. However, for orbital ripples, the ripple steepness is a constant, and the Keulegan–Carpenter number defined using either ripple wavelength and ripple height gives the same conclusion. For cases with the same ripple steepness but different ripple wavelengths (kc0.8s1.0, kc1.0s1.0 and kc1.2s1.0), it is found that Γ_v and averaged Γ_v per ripple wavelength are largest when the parameter K_C is around the value of K_{C0}. For a specific ripple steepness, our results suggest that there exists an optimized condition in ripple wavelength for a maximum circulation (vortex strength flux) per unit ripple wavelength or the strongest columnar coherent vortex. This ripple wavelength is consistent with commonly observed equilibrium orbital ripples.

3.3. *Bottom shear stress on oscillatory flow*

Similar to the flat bed scenario, there is a skin friction contribution to the bottom shear stress experienced by the overlying oscillatory flow. Bottom shear stress due to skin friction is directly related to the fluid viscosity as the flow moves over the no-slip surface of the bed.

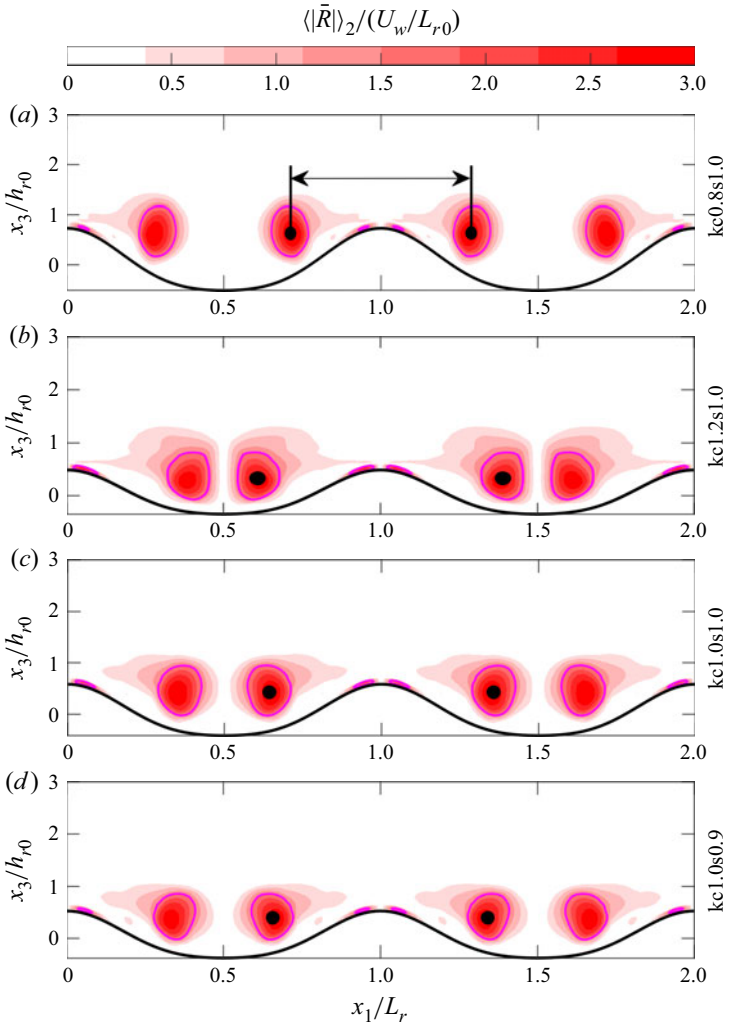

Figure 10. Strength of the time-averaged vortex vector filed $\langle|\bar{\boldsymbol{R}}|\rangle_2$ after the normalization by U_w/L_{r0}. The purple contour lines correspond to the criterion $\langle|\bar{\boldsymbol{R}}|\rangle_2/(U_w/L_{r0}) = 1.5$. The black solid circle marks the location of weighted centre. Results of two ripples are presented for illustration.

However, when a vortex ripple bed appears, there is a significant spatial inhomogeneity in the local boundary layer flow due to the generation and evolution of coherent vortices (illustrated in figure 6), which alters the pressure distribution on the ripple flanks. As a result, a ripple-averaged force caused by the pressure gradient in the streamwise direction is produced, which is often referred to as the form drag. Bottom shear stress due to form drag is usually much stronger than the skin friction, such that the presence of vortex ripples significantly enhances the local flow resistance (Yuan & Wang 2018). Through numerical simulations, the ripple-averaged bottom shear stress experienced by the flow over ripples with different dimensions is thoroughly studied in this section.

The ripple-averaged total bottom shear stress quantifies how much resistance (skin friction and form drag) in total the bedform exerts on the overlying flow. Based on the stress tensor $\sigma_{ij} = -p\delta_{ij} + \tau_{ij}$, the ripple-averaged total bottom shear stress (i.e. the shear

stress experienced by the flow) is calculated as

$$\langle \tau_t \rangle_w = \langle \boldsymbol{n}_1^{\mathrm{T}} \cdot \boldsymbol{\sigma} \cdot \boldsymbol{n}_n \rangle_w, \tag{3.10}$$

where the superscript T denotes the transpose of a vector, the unit directional vector $\boldsymbol{n}_1 = [1\ 0\ 0]^{\mathrm{T}}$ is in streamwise direction and $\boldsymbol{n}_n$ is perpendicular to the surface of ripple which reads

$$\boldsymbol{n}_n = \frac{\left[-\dfrac{\partial \eta_r}{\partial x_1} \quad -\dfrac{\partial \eta_r}{\partial x_2} \quad 1\right]^{\mathrm{T}}}{\sqrt{1 + \left(\dfrac{\partial \eta_r}{\partial x_1}\right)^2 + \left(\dfrac{\partial \eta_r}{\partial x_2}\right)^2}}. \tag{3.11}$$

In a similar way but using only the viscous stress tensor τ_{ij} instead of σ_{ij}, the skin friction component in the total bottom shear stress is calculated as

$$\langle \tau_s \rangle_w = \langle \boldsymbol{n}_1^{\mathrm{T}} \cdot \boldsymbol{\tau} \cdot \boldsymbol{n}_n \rangle_w. \tag{3.12}$$

Accordingly, the form drag component of bottom shear stress is calculated as $\langle \tau_f \rangle_w = \langle \tau_t - \tau_s \rangle_w$, such that only the dynamic pressure tensor is involved in the calculation of $\langle \tau_f \rangle_w$. The ripple-averaged total bottom shear stress $\langle \tau_t \rangle_w$, skin friction component $\langle \tau_s \rangle_w$ and form drag component $\langle \tau_f \rangle_w$ of bottom shear stress are respectively computed for each case and their evolutions throughout one wave cycle, are shown in figure 11. For all cases investigated in this study, the total bottom shear stress shows a slight phase lead with respect to the free-stream velocity (compare solid lines in figure 11*b* with panel *a*). Specifically, a significant phase advance of around $\pi/4$ relative to the free-stream velocity is found in the skin friction component of bottom shear stress (dashed lines in figure 11*b*). Phase lead of the bottom shear stress in a turbulent wave bottom boundary layer over a flat bed is well established (Spalart & Baldwin 1989; Cheng *et al.* 2015; Yue *et al.* 2020) and the nearly $\pi/4$ phase lead in $\langle \tau_s \rangle_w$ is consistent with the laminar flow solution. The low magnitude of $\langle \tau_s \rangle_w$ and its laminar-like feature suggest that the form drag component $\langle \tau_f \rangle_w$ dominates the total bottom stress. The form drag bottom shear stress is shown in figure 11(*c*), which indeed shows dominance in the total bottom shear stress when comparing the magnitudes between $\langle \tau_f \rangle_w$ and $\langle \tau_s \rangle_w$. Thus, it is reasonable to find that the form drag $\langle \tau_f \rangle_w$ is also relatively in phase with the free-stream velocity. Three instants during a wave cycle are of interest, which are marked as the triangles, circles and squares in figure 11(*a*,*c*). These three instants are when the form drag component of bottom shear stress $\langle \tau_f \rangle_w$ is zero or at peaks, and they are respectively grouped as ① to ③ in figure 11(*c*) and their phase values θ are listed in table 4.

The two peaks, i.e. group ② and ③, in the form drag component of bottom shear stress are important features as laboratory measurements, e.g. Yuan & Wang (2018, 2019) suggest that these peaks are closely related to coherent vortex motions discussed in the previous section. The inter-relationships between vortex motion, dynamic pressure and form drag are illustrated in figure 12, where the turbulence-averaged spanwise vorticity and pressure fields are respectively presented in panels (*a*,*c*,*e*) and (*b*,*d*,*f*), along with the cross-ripple distribution of form drag bottom shear stress in panels (*b*,*d*,*f*). As before, the purple contour lines in figure 12 denote the primary vortices detected by the normalized vortex strength criterion $\langle |\boldsymbol{R}| \rangle_{p2}/(U_w/L_{r0}) = 3$. The results for the wave phase in group ① are also presented for comparison and completeness. At the instant when $\langle \tau_f \rangle_w = 0$, the negative pressure region coincides with the developing primary vortex and it is detached from the ripple surface (figure 12*b*). This feature is consistent with the nearly

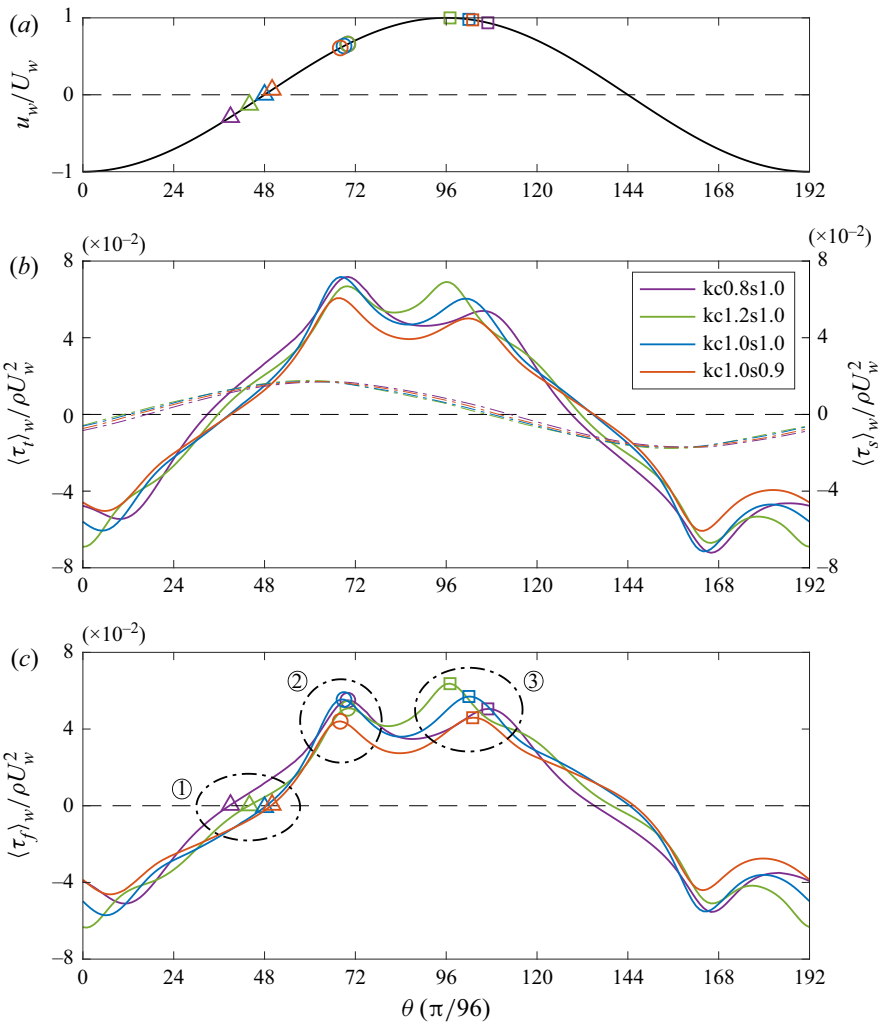

Figure 11. Evolution of the ripple-averaged bottom shear stress throughout one wave cycle: (*a*) the free-stream velocity u_w normalized by U_w; (*b*) the total bottom shear stress $\langle\tau_t\rangle_w$ denoted by solid lines and the skin friction bottom shear stress $\langle\tau_s\rangle_w$ denoted by dash-dot lines; (*c*) the form drag bottom shear stress $\langle\tau_f\rangle_w$. All the bottom shear stresses are normalized by ρU_w^2. Three wave phases are respectively marked as triangles, circles and squares, grouped as ① to ③ in (*c*), corresponding to the wave phases when the form drag bottom shear stresses are zeros or at their peaks. These wave phases are also illustrated in (*a*).

zero ripple-averaged form drag bottom shear stress. At the first peak in $\langle\tau_f\rangle_w$, which corresponds to figure 12(*c*) (between $\theta = 67\pi/96$ to $70\pi/96$ for different cases), the primary vortex is just above the ripple crest and it is about to be ejected into the water column along with the secondary vortex. Under the influence of this vortex dipole, the flow near the ripple crest is significantly enhanced and its magnitude is comparable to the amplitude of free-stream velocity. Compared with figure 12(*b*), the pressure field in figure 12(*d*) attaches to the ripple surface. Illustrated by the distribution of τ_f over one ripple wavelength, the pressure on ripple surface produces a strong and positive net pressure drag on the overlying flow in the streamwise direction. At the instants right after the positive flow peak around $97\pi/96$ to $107\pi/96$ in wave phase, the free-stream velocity

Case	kc0.8s1.0	kc1.2s1.0	kc1.0s1.0	kc1.0s0.9
Group ① in figure 11 (triangle)	39	44	48	50
Group ② in figure 11 (circle)	70	70	69	68
Group ③ in figure 11 (square)	107	97	102	103
First peak in figure 13 (circle)	69	69	67	66
First peak in figure 14 (circle)	69	69	67	66
First peak in figure 15 (circle)	69	69	67	66
Second peak in figure 13 (square)	104	95	100	100
Second peak in figure 14 (square)	102	95	99	100
Second peak in figure 15 (square)	105	96	100	101

Table 4. The detected wave phases in unit of $\pi/96$.

has just passed its maximum value, and the flow separation at the ripple crest produces a new primary coherent vortex in the lee side (on right flank of the ripple), which is closely attached to the ripple surface (figure 12*e*). It is evident that the dynamic pressure is low within the lee vortex, so the pressure difference between the two ripple flanks can produce a large horizontal net pressure gradient. The flow deceleration leads to this unfavourable pressure gradient, which can further enhance flow separation and vortex development (Yuan & Wang 2018). It should be noted that, from figure 11(*c*) and table 4, there is a notable phase difference among the instants when group ① to ③ occur for each of the four cases. This implies that, although the four cases investigated in this study have similar coherent vortex motions, the difference in ripple dimensions can evidently alter the timing of these characteristic motions that occur. More quantitative discussions are given in the next section.

3.4. *Shear stress on ripple surface*

In §§ 3.1–3.3, the dynamics of the overlying flow is studied in detail through the evolution of the coherent vortex and the bottom shear stress induced by the bedform for a rippled bed with different dimensions but subjected to the same oscillatory motion. In this section, we investigate the spatial distribution of shear stress on ripple surface and the implied role in sediment transport from multiple perspectives.

Similar to the expression in (3.10) and (3.12) for the bottom shear stress on overlying flow, the shear stress (felt by the ripple) locally tangent to the ripple surface is calculated based on the stress tensor, which is expressed as

$$\tau_{bi} = \boldsymbol{n}_{ti}^{\mathrm{T}} \cdot \boldsymbol{\tau} \cdot \boldsymbol{n}_n, \tag{3.13}$$

where the subscript $i = 1$ or 2. The unit directional vector $\boldsymbol{n}_n$ defined in (3.11) is perpendicular to ripple surface, while $\boldsymbol{n}_{ti}$ is tangential to the surface which reads

$$\boldsymbol{n}_{t1} = \frac{\left[1 \quad 0 \quad \dfrac{\partial \eta_r}{\partial x_1}\right]^{\mathrm{T}}}{\sqrt{1 + \left(\dfrac{\partial \eta_r}{\partial x_1}\right)^2}} \quad \text{and} \quad \boldsymbol{n}_{t2} = \frac{\left[0 \quad 1 \quad \dfrac{\partial \eta_r}{\partial x_2}\right]^{\mathrm{T}}}{\sqrt{1 + \left(\dfrac{\partial \eta_r}{\partial x_2}\right)^2}}. \tag{3.14a,b}$$

Here, we consider the strength of total shear stress on the ripple surface to be quantified by its magnitude. The evolution of the phase- and ξ_2-averaged amplitude of total bottom

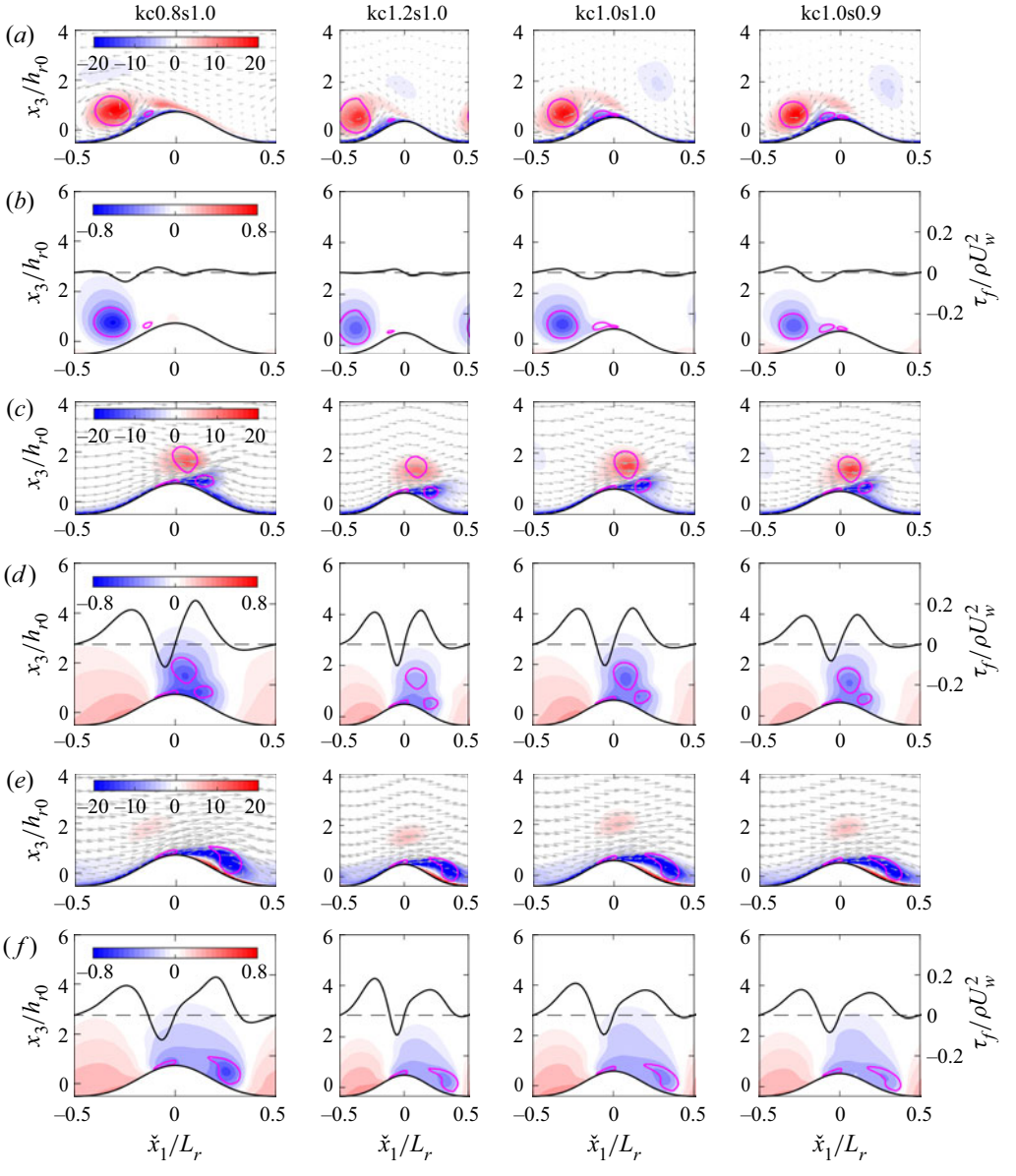

Figure 12. Turbulence-averaged flow fields at the three wave phases grouped in figure 11: (*a*,*c*,*e*) the normalized turbulence-averaged velocities $(\langle u_1\rangle_{p2}, \langle u_3\rangle_{p2})/U_w$ presented as a vector field denoted by the grey arrows, and the normalized spanwise vorticity $\langle\omega_2\rangle_{p2}/(U_w/L_{r0})$ which is presented as iso-surfaces, respectively corresponding to the groups ① to ③; (*b*,*d*,*f*) the normalized turbulence-averaged pressure $\langle p\rangle_{p2}/\rho U_w^2$ which is presented as iso-surfaces, respectively corresponding to the groups ① to ③. The distribution of normalized form drag bottom shear stress $\tau_f/\rho U_w^2$ is also presented in (*b*,*d*,*f*). The coherent vortices are identified using the vortex vector method as the purple contour lines, where the normalized vortex strength criterion is $\langle|\boldsymbol{R}|\rangle_{p2}/(U_w/L_{r0}) = 3$. The local ripple coordinate $\check{x}_1$ is employed and the dashed lines are plotted for reference.

shear stress $\langle|\tau_b|\rangle_{p2}$ on the ripple surface throughout one wave cycle is shown in figure 13. In addition to the shear stress, trajectories of the primary vortices detected in figure 6 are also presented. From figure 13, it is clear that the region of intense shear stress $\langle|\tau_b|\rangle_{p2}$ is roughly enclosed by the vertical projection of the primary vortex before it moves across

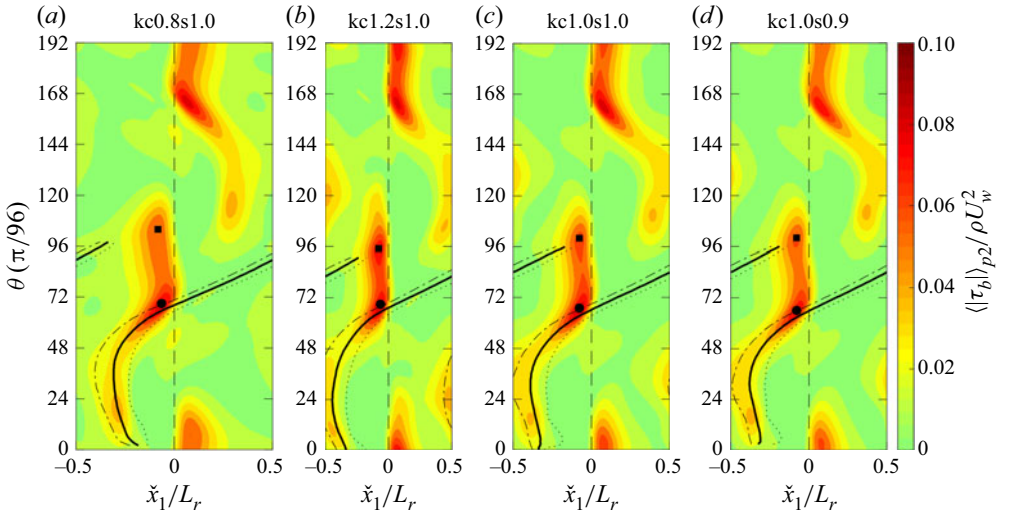

Figure 13. Evolution of the phase- and ξ_2-averaged amplitude of total shear stress $\langle|\tau_b|\rangle_{p2}$ on the ripple surface throughout one wave cycle, after the normalization by ρU_w^2. The solid circles and squares mark the two peaks in the distribution of $\langle|\tau_b|\rangle_{p2}$. The dash-dot, thick solid and dot lines are respectively the trajectories of the far-left, weighted centre and far-right points on the primary vortices, which are detected by the normalized vortex strength criterion $\langle|\boldsymbol{R}|\rangle_{p2}/(U_w/L_{r0}) = 3$. For a clear presentation, these trajectories are only shown for the first half-wave cycle. The local ripple coordinate $\check{x}_1$ is employed and the dashed lines mark the streamwise location of ripple crests.

the ripple crest toward the opposite side of the ripple. This observation indicates that, before the ejection, the primary vortex has a clear footprint on the ripple surface as it is close to the rippled bed within a region below $\xi_3 = 1.2h_{r0}$ (figure 8*b*). This feature can also be verified by the intense up-ripple flow induced by the primary vortex shown in figure 12(*a*,*c*). Because of the interaction between the primary vortex and ripple surface, during this period, the intense region of $\langle|\tau_b|\rangle_{p2}$ in case kc0.8s1.0 is found to be relatively close to the ripple crest ($\check{x}_1/L_r$ between -0.35 to -0.2) while in case kc1.2s1.0, this region is relatively far from the ripple crest ($\check{x}_1/L_r$ near -0.5). The location of this intense region is insensitive to ripple steepness (the locations are almost the same for kc1.0s1.0 and kc1.0s0.9), which is consistent with that illustrated in figure 6. Relatively, the primary vortex can travel further towards or even slightly beyond the ripple trough with a larger K_C, which shows less dependence on the ripple steepness. In spite of these differences, primary vortices in these four cases are ejected from the ripple crest at a similar wave phase around $66\pi/96$ to $69\pi/96$. Meanwhile, marked as solid circles, peaks in the distribution of $\langle|\tau_b|\rangle_{p2}$ are found on the left ripple flank immediately adjacent to the ripple crest. After the vortex ejection, we can no longer see any notable vortex signature on the stress over the ripple surface. Moreover, it takes more than approximately $26\pi/96$ in wave phase for the primary vortices to reach their destruction by viscous dissipation at a location near the adjacent ripple crest on the right-hand side. Close to the time when the ejected primary vortex is finally dissipated and through its interaction with the neighbour ripple crest (see figure 12(*e*) for the light red regions), a second peak (marked as solid squares) near the ripple crest in the total shear stress is also observed. The wave phases that correspond to these two peaks in the distribution of $\langle|\tau_b|\rangle_{p2}$ are listed in table 4, where a notable divergence in wave phase is found for the second peak. The divergence in the timing of the second peak is clearly caused by the difference in ripple wavelength specified in

these cases. Since the high shear stress region near the stoss side of the ripple crest around the peak flow interval (wave phase between $60\pi/96$ to $120\pi/96$) is responsible for major sediment transport and onshore ripple migration in velocity skewed waves (e.g. van der Werf *et al.* 2007), a more complete discussion on the mechanisms causing the large total shear stress and its two local peaks will be analysed later using components due to averaged flow, ripple-induced fluctuation and turbulent fluctuation. It takes a longer time for the ejected primary vortex to reach an adjacent ripple in case kc0.8s1.0 where $L_r = 1.25\,L_{r0}$, and a shorter time in kc1.2s1.0 where $L_r = 0.8\,L_{r0}$. This also implies that the travelling speed of these ejected primary vortices is similar.

In order to measure the amount of force induced by flow shear over the ripples, integration of the time-averaged magnitude of total shear stress over the ripple surface is taken, which reads

$$f_\tau = \int_0^{L_r} \langle \overline{|\tau_b|} \rangle_2 \sqrt{1 + (\partial \eta_r/\partial x_1)^2}\, \mathrm{d}x_1. \tag{3.15}$$

The force f_τ quantifies the time-averaged flow shear stress felt by the ripple surface, which may also be considered as an indicator for the amount of sediment erosion on ripple surface. The value of f_τ for each of the four cases analysed in this study is listed in table 2. After averaging over one ripple wavelength, the corresponding normalized value is provided in table 3. From the normalized values shown in table 3, it is remarkable to find that increasing or decreasing the ripple wavelength from its equilibrium value exerts more shear stress per unit area on the ripple surface (case kc1.0s1.0 has a smaller f_τ/L_r than cases kc0.8s1.0 and kc1.2s1.0). Furthermore, reducing the ripple height from the equilibrium value (compare data from case kc1.0s0.9 with kc1.0s1.0) also reduced the shear stress experienced by the ripple. A similar conclusion is obtained for the ripple-averaged total bottom shear stress on overlying flow. The total time- and ripple-averaged stress $\overline{|\langle \tau_t \rangle_w|}$ is also calculated and listed in table 3. Similar to f_τ/L_r, $\overline{|\langle \tau_t \rangle_w|}$ shows that the overlying flow experiences more drag when changing the ripple wavelength from the equilibrium value. The numerical investigation using four different ripple dimensions subject to the same oscillatory flow suggests that the total shear stress felt by ripple surface is minimized at the equilibrium ripple wavelength. On the other hand, the enhanced ripple height causes greater flow resistance and total shear stress due to stronger spanwise vortices.

Evolution of the shear stress on ripple surface throughout one wave cycle is examined in figure 14 by analysing the components contributed by the turbulent fluctuation and turbulence-averaged flow separately. The shear stress induced by turbulent motion, shown in figure 14(*a*), is quantified by the intensity of its turbulent fluctuating component $\langle |\tau_b'| \rangle_{p2}$, where the amplitude of the fluctuating shear stress is defined as

$$|\tau_b'| = \sqrt{{\tau_{b1}'}^2 + {\tau_{b2}'}^2}. \tag{3.16}$$

Correspondingly, shear stress carried by the turbulence-averaged flow is calculated and the streamwise component $\langle \tau_{b1} \rangle_{p2}$ is presented in figure 14(*b*). Trajectories of the detected primary vortex in figure 6 are also presented. Similar to the finding from figure 13, the primary vortex has a clear footprint on both distributions of the turbulent-fluctuating and turbulence-averaged shear stresses over ripple surface. By comparing the magnitudes of the two components, all four cases indicate that the turbulence-averaged streamwise shear stress component makes a greater contribution to the total shear stress with a more organized pattern. The region of higher intensity of $\langle |\tau_b'| \rangle_{p2}$ is still associated with the primary vortex motion, although less organized. Moreover, in terms of the peak values,

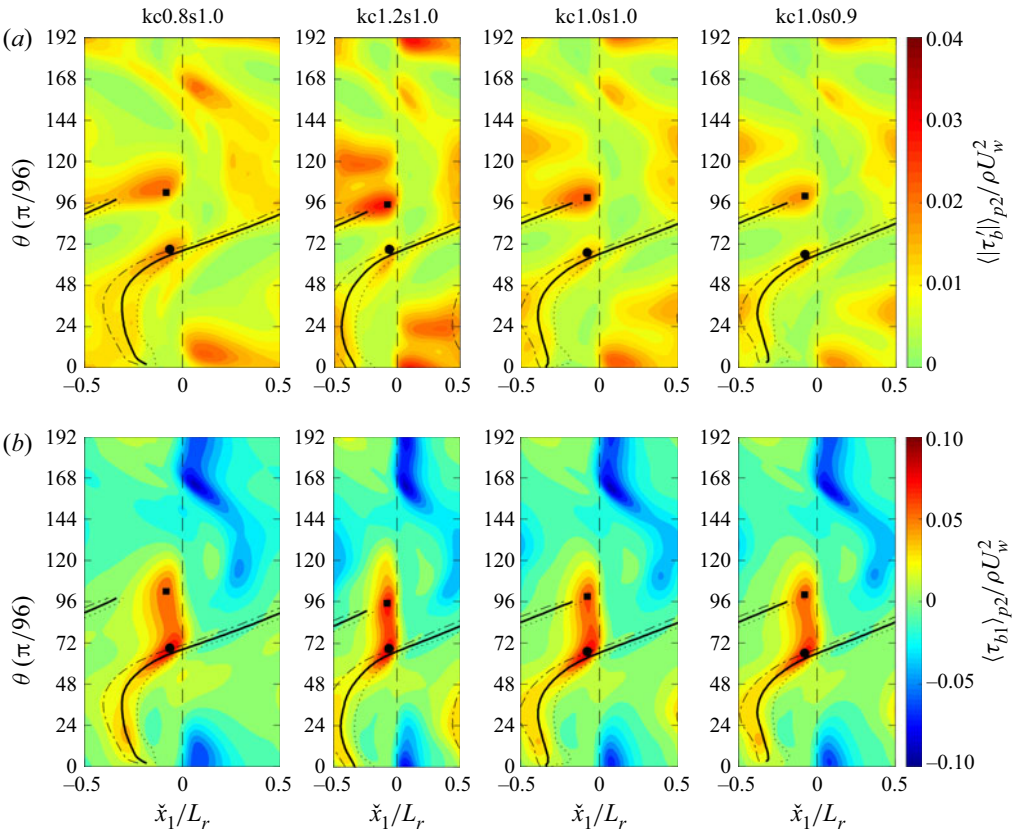

Figure 14. Evolution of shear stress on the ripple surface throughout one wave cycle: (*a*) the intensity of turbulent-fluctuation component $\langle|\tau_b'|\rangle_{p2}$; (*b*) the turbulence-averaged streamwise component $\langle\tau_{b1}\rangle_{p2}$. The solid circles and squares mark the two peaks in the distribution of $\langle\tau_{b1}\rangle_{p2}$. All wall shear stress components are normalized by ρU_w^2. The dash-dot, thick solid and dot lines are respectively the trajectories of the far-left, weighted centre and far-right points on the primary vortices, which are detected by the normalized vortex strength criterion $\langle|\boldsymbol{R}|\rangle_{p2}/(U_w/L_{r0}) = 3$. For a clear presentation, these trajectories are only shown for the first half wave cycle. The local ripple coordinate $\check{x}_1$ is employed and the dashed lines mark the streamwise location of ripple crests.

$\langle|\tau_b'|\rangle_{p2}$ are generally a factor two or three smaller than $\langle|\tau_{b1}|\rangle_{p2}$. Intense streamwise shear stress is detected at a connected and concentrated region from the early stage of vortex formation. Especially, from wave phase $\theta = 60\pi/96$ to $120\pi/96$, there is an evident enhancement in $\langle\tau_{b1}\rangle_{p2}$ located close to the ripple crest on the left ripple flank. During this period, two peaks in the turbulence-averaged streamwise shear stress are found and respectively marked as solid circles and squares. As shown in table 4, the two peaks in $\langle\tau_{b1}\rangle_{p2}$ actually have very similar waves phases to the peaks detected in figure 13. This further confirms that the turbulence-averaged streamwise shear stress dominates the total shear stress on the ripple surface. Locations of the two peaks are also marked in figure 14(*a*), which are found to be close to the local maximum in the turbulent-fluctuating shear stress.

The turbulence-averaged streamwise shear stress on the ripple surface shown in figure 14(*b*) can be further decomposed into a component due to ripple-averaged flow $\langle\tau_{w1}\rangle_{p2}$ (figure 15*a*) and the other component due to ripple-induced fluctuation $\langle\tau_{r1}\rangle_{p2}$

(figure 15*b*). Following the expression of (3.13), the stresses τ_{w1} and τ_{r1} read

$$\tau_{w1} = \boldsymbol{n}_{t1}^{\mathrm{T}} \cdot \boldsymbol{\tau}_w \cdot \boldsymbol{n}_n \quad \text{and} \quad \tau_{r1} = \boldsymbol{n}_{t1}^{\mathrm{T}} \cdot \boldsymbol{\tau}_r \cdot \boldsymbol{n}_n, \tag{3.17a,b}$$

where the stress tensors $\tau_{wij} = 2\mu S_{wij}$ and $\tau_{rij} = 2\mu S_{rij}$, with

$$S_{wij} = \frac{1}{2}\left(\frac{\partial \langle u_i \rangle_w}{\partial x_j} + \frac{\partial \langle u_j \rangle_w}{\partial x_i}\right) \quad \text{and} \quad S_{rij} = \frac{1}{2}\left(\frac{\partial \langle u_i \rangle_r}{\partial x_j} + \frac{\partial \langle u_j \rangle_r}{\partial x_i}\right). \tag{3.18a,b}$$

For a clear comparison, trajectories of the primary vortex are also presented as lines, with the solid circles and squares marking the positions of the peak stress due to ripple-induced fluctuation. By comparing the magnitudes between $\langle \tau_{w1} \rangle_{p2}$ and $\langle \tau_{r1} \rangle_{p2}$, it is clear that the shear stress on the ripple surface due to ripple-induced fluctuation is greater than that caused by ripple-averaged flow. As we have demonstrated in figure 14, the turbulence-averaged shear stress plays a major role in the total shear stress on the ripple surface. As a result, the shear stress caused by the ripple-induced fluctuation $\langle \tau_{r1} \rangle_{p2}$ is the dominating component in the total shear stress over the ripple surface. Consequently, the wave phases that correspond to the two peaks in figures 13–15 are very close to one another (see table 4). In addition to their magnitudes, the evolution of $\langle \tau_{w1} \rangle_{p2}$ and $\langle \tau_{r1} \rangle_{p2}$ is also different. The stress $\langle \tau_{w1} \rangle_{p2}$ peaks right before the ejection of primary vortex (marked as the circles in figure 15*a*), with an advance approximately $32\pi/96$ in wave phase relative to the peak of the free stream. Meanwhile, $\langle \tau_{w1} \rangle_{p2}$ tends to cover the whole ripple surface with a more homogeneous distribution. As the ripple-induced fluctuation takes the majority of the turbulence-averaged shear stress over the ripple surface, footprints of the primary vortex in figure 15(*b*) are clearly recognizable. Enhancement in the ripple-induced shear stress is also clearly detectable on the stoss side of the ripple flank.

The regions with intense shear over ripple surface are of most practical interest as they imply regions prone to active sediment motion. Therefore, we will focus on the turbulence-averaged streamwise shear stress hereafter. As we explained previously in figure 14, the two peaks in $\langle \tau_{b1} \rangle_{p2}$ relate to the evolution of primary vortex. But between the two peaks, we still can observe an enhancement in $\langle \tau_{b1} \rangle_{p2}$ on a ripple flank close to the ripple crest. The enhancement is found to be caused by the accelerating upstream boundary layer flow covering the stoss-side ripple flank (Charru *et al.* 2013). This is illustrated in figure 16, where the turbulence-averaged velocities during the mid-jet-ejection stage are presented at the wave phase $80\pi/96$. The streamwise component is shown in figure 16(*a*), where the purple lines denote the primary vortices detected in figure 6. From the figure, it is observed that the ejected primary vortex is still over a trough on its way toward the adjacent ripple crest, and there is a local peak in the streamwise velocity field near the ripple crest. Along with the vertical velocity component shown in figure 16(*b*), the flow on the left ripple flank is found to accelerate upstream of the ripple crest, creating the intense shear in the region very close to the ripple surface. Note that the magnitude of $\langle u_1 \rangle_{p2}$ is much larger than $\langle u_3 \rangle_{p2}$ and the corresponding velocity vector field is shown in figure 6(*e*). Laboratory experiments with sediment transport, such as van der Werf *et al.* (2007), Frank-Gilchrist *et al.* (2018) and Wang & Yuan (2020), show that this intensified shear stress erodes sediment in the stoss side and creates a strong sediment flux toward the ripple crest and the lee side of the ripple. The thick lines in figure 16(*b*) are the corresponding turbulence-averaged streamwise components of the shear stress on the ripple shown in figure 14(*b*). The distribution of $\langle \tau_{b1} \rangle_{p2}$ on ripple surface shows a phase advance compared with the ripple topography, namely the maximum wall shear stress is located slightly upstream of the crest. A similar finding is reported in unidirectional flows over a bedform (Charru *et al.* 2013).

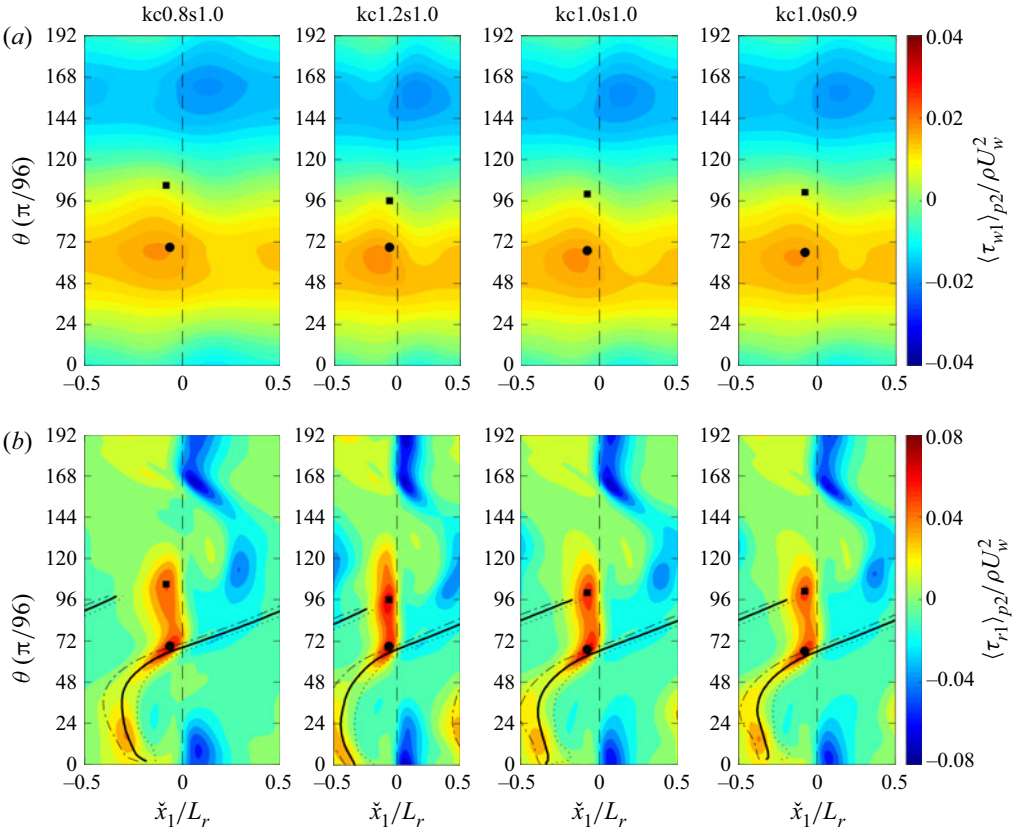

Figure 15. Evolution of the turbulence-averaged shear stress on the ripple surface throughout one wave cycle: (*a*) the component carried by the ripple-averaged wave-induced motion $\langle\tau_{w1}\rangle_{p2}$; (*b*) the component carried by the ripple-induced fluctuation $\langle\tau_{r1}\rangle_{p2}$. The solid circles and squares mark the two peaks in the distribution of $\langle\tau_{r1}\rangle_{p2}$. All wall shear stress components are normalized by ρU_w^2. The dash-dot, thick solid and dot lines are respectively the trajectories of the far-left, weighted centre and far-right points on the primary vortices, which are detected by the normalized vortex strength criterion $\langle|\boldsymbol{R}|\rangle_{p2}/(U_w/L_{r0}) = 3$. For a clear presentation, these trajectories are only shown for the first half-wave cycle. The local ripple coordinate $\check{x}_1$ is employed and the dashed lines mark the streamwise location of the ripple crests.

More analysis of the accelerating boundary layer flow in the stoss side of the ripple (upstream of ripple crest) is taken based on the triple-decomposition equation (2.15). From formula $\langle\psi\rangle_r = \langle\psi\rangle_{p2} - \langle\psi\rangle_w$, the ripple-induced fluctuation $\langle\psi\rangle_r$ can be understood in a similar way as the 'same-elevation speed-up' (the difference between the actual velocity and the unperturbed velocity at the same elevation above the bottom wall) concept proposed by Charru & Franklin (2012). Here, the ripple-averaged flow over a ripple $\langle\psi\rangle_w$ is taken as a phase-dependent reference, which is required to be independent of the streamwise location. The resultant ripple-induced fluctuation $\langle\psi\rangle_r$ thus represents a 'speed-up' in the turbulence-averaged flow caused by the spatial inhomogeneity of bedform. To strengthen our explanation, the ripple-induced velocity fluctuations at the wave phase $80\pi/96$ are presented in figure 17, which can be contrasted with the turbulence-averaged velocities shown in figure 16. The streamwise component of velocity fluctuation is illustrated in figure 17(*a*) with the detected coherent vortices shown in purple

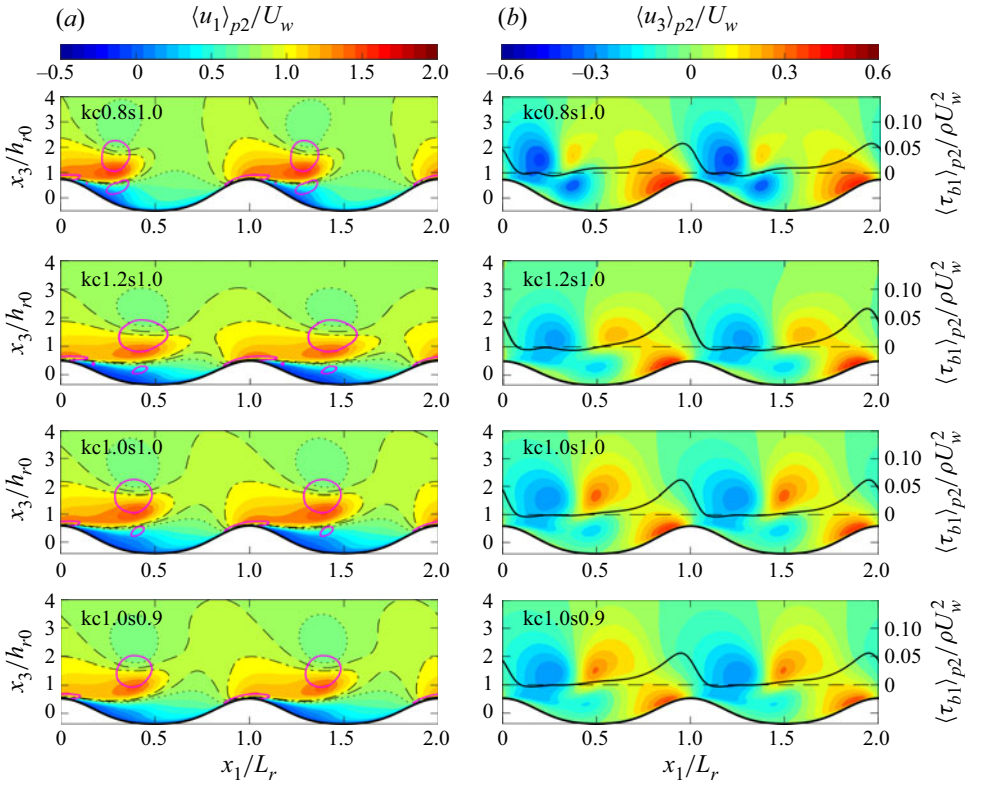

Figure 16. Turbulence-averaged velocity field during the jet-ejection stage at the wave phase $80\pi/96$. (*a*) The normalized turbulence-averaged streamwise velocity field $\langle u_1\rangle_{p2}/U_w$. The dot, dashed and dash-dot lines correspond to the iso-values of 0.8, 0.9 and 1.0 in units of U_w, respectively. The purple contour lines denote the vortices detected by the normalized vortex strength criterion $\langle|\boldsymbol{R}|\rangle_{p2}/(U_w/L_{r0}) = 3$. (*b*) The normalized turbulence-averaged vertical velocity field $\langle u_3\rangle_{p2}/U_w$. The thick lines are the corresponding normalized turbulence-averaged streamwise components of the shear stress $\langle\tau_{b1}\rangle_{p2}/\rho U_w^2$, while the dashed lines correspond to the reference. Results of two ripples are presented for illustration.

contour lines. An intensification of ripple-induced streamwise velocity of the order of U_w is observed around the ripple crest. From the velocity field $\langle u_1\rangle_r$, a clear speed-up around the ripple crest is observed, which imposes a stronger shear stress on the ripple surface as shown in figure 15(*b*). The spatial fluctuation of the streamwise velocity is confined to the near-bed region. The corresponding velocity is positive upstream and right on the ripple crest while it is mainly negative downstream of the ripple crest (lee side of the ripple). This feature is consistent with flow separation and similar features are captured in a laboratory experiment through a double-averaging procedure (Hare *et al.* 2014). The corresponding vertical velocity fluctuation is illustrated in figure 17(*b*), where the solid line corresponds to the turbulence-averaged shear stress $\langle\tau_{b1}\rangle_{p2}$ in figure 16(*b*) while the thick dash-dot line denotes its ripple-induced component shown in figure 15(*b*). Evidently, we find that the distribution of $\langle\tau_{r1}\rangle_{p2}$ follows $\langle\tau_{b1}\rangle_{p2}$ on the ripple surface but with a negative shift, which confirms that, the shear stress on ripple surface caused by turbulence-averaged flow has a relatively uniform distribution over one ripple wavelength illustrated in figure 15(*a*).

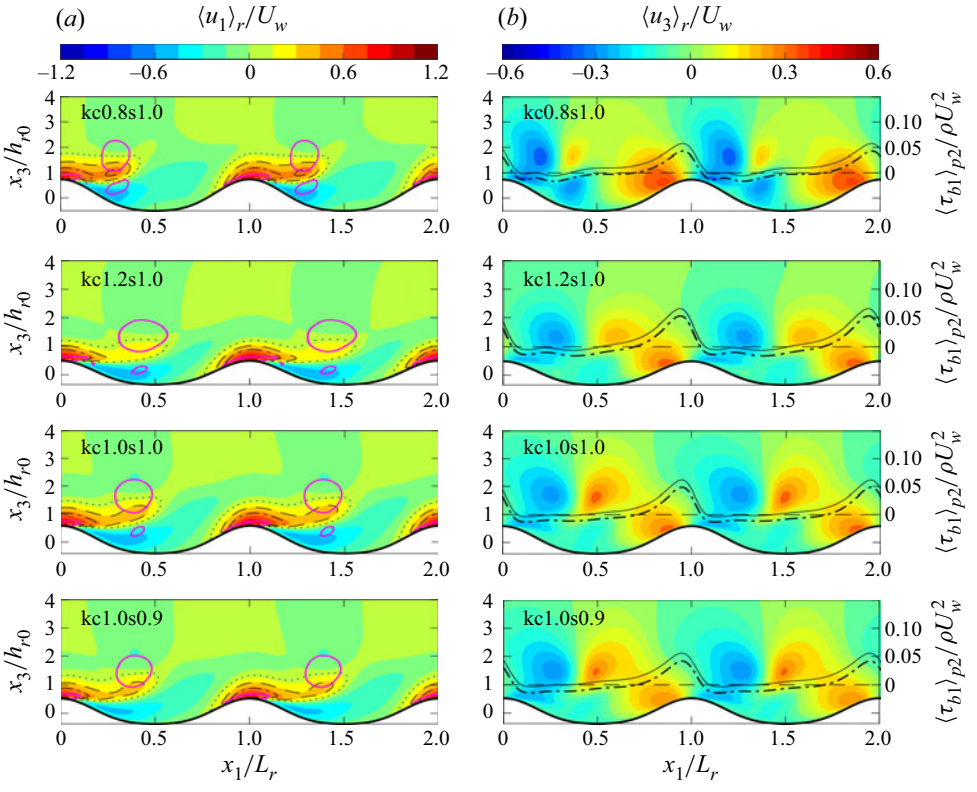

Figure 17. Turbulence-averaged velocity field carried by the ripple-induced fluctuation during the jet-ejection stage at the wave phase $80\pi/96$. (*a*) The normalized turbulence-averaged ripple-induced streamwise velocity fluctuation $\langle u_1\rangle_r/U_w$. The dot, dashed and dash-dot lines correspond to the iso-values of 0.1, 0.3 and 0.5 in units of U_w, respectively. The purple contour lines denote the vortices detected by the normalized vortex strength criterion $\langle|\boldsymbol{R}|\rangle_{p2}/(U_w/L_{r0}) = 3$. (*b*) The normalized turbulence-averaged ripple-induced vertical velocity fluctuation $\langle u_3\rangle_r/U_w$. The solid lines are the normalized turbulence-averaged streamwise component of the shear stress over the ripple surface $\langle\tau_{b1}\rangle_{p2}/\rho U_w^2$, while the thick dash-dot lines represent the corresponding component carried by the ripple-induced fluctuation. The dashed lines correspond to the reference zero. Results of two ripples are presented for illustration.

4. Discussion

According to our previous analysis in § 3, the trajectory and time-averaged strength of coherent vortex, and the magnitude of total shear stress on the ripple surface (or bottom shear stress on overlying flow) are the two key factors in the selection of ripple dimensions. Here, based on these two factors, we propose a mechanism in the selection of vortex ripple height and wavelength, or the governing parameters s and K_C. As the ripple height increases from case kc1.0s0.9 where $h_r = 0.9h_{r0}$ to the equilibrium case kc1.0s1.0 where $h_r = 1.0h_{r0}$, the vortex strength flux increases by more than 10 % to a maximum value around $\Gamma_v = 0.25\ U_wL_{r0}$. Therefore, vortex strength is regarded to be one of the key factors in the selection of ripple steepness s. In other words, equilibrium vortex ripples prefer stronger ripple-averaged coherent vortex strength, which leads to a larger ripple height. Then, the maximum ripple height is determined by a balance of vortex motion and sediment avalanche (Salimi-Tarazouj *et al.* 2021). The factors that further limit ripple steepness must be investigated by also considering the sediment transport, including the effects of sediment grain diameter (Dimas & Leftheriotis 2019) and grain

size sorting (Black & Oldman 1999). However, this cannot be addressed by the present model. Nevertheless, we note that by increasing ripple steepness, the total shear stress is also increased in this process (see figure 13), which could play a role in limiting the ripple steepness s from continuously increasing because of stronger bed erosion around the ripple crests along with the avalanche mechanism (i.e. gravity effects). This conjecture leads to the next important conclusion regarding the selection of ripple wavelength for a given steepness. By increasing (case kc0.8s1.0) or decreasing (kc1.2s1.0) the ripple wavelength from the equilibrium condition (case kc1.0s1.0) but keeping the same ripple steepness, we obtain larger bottom shear stress experienced by the overlaying flow and stronger shear stress experienced by the ripple surface. In fact, bottom shear stress experienced by the flow and shear stress felt by the ripple are correlated, and the larger values correspond to stronger bottom friction and sediment transport, respectively. Thus, compared with vortex strength flux, the total shear stress experienced by the ripple is regarded to be the dominant factor in the selection of parameter K_C. For a given oscillatory flow, the equilibrium ripple wavelength exists such that the overlying flow tends to feel a smaller drag and the ripple surface tends to experience a lower shear stress (implying less sediment transport). In summary, during the selection process of ripple dimensions, the interaction between the overlying flow and ripples tends to generate stronger coherent vortices while, in the meantime, the ripple surface prefers a smaller shear stress. In practice, the selection of vortex ripple height and wavelength actually happens simultaneously, characterized by the trajectory of coherent vortices and the corresponding signature in shear stress on ripple surface. Therefore, there is an evident advantage if we can take both the two factors at the same time, i.e. the coherent vortex and the total shear stress, into our consideration in understanding the selection of ripple dimensions. As a result, the ripple-induced fluctuation defined in (2.15), is worth investigating since it carries the coherent vortices and the majority of shear stress simultaneously.

5. Conclusions

In this study, we have performed DNSs of sinusoidal oscillatory flow over out-of-equilibrium vortex ripples to study the fluid dynamical controls (not sediment dynamics) in determining their distinctive equilibrium dimensions. The case C2 in Önder & Yuan (2019) for oscillatory flow over equilibrium orbital ripples is selected as the reference of equilibrium. By altering the ripple wavelength and height from their equilibrium values, three other cases have been carried out and differences in flow kinematics are observed. In comparison with the equilibrium case, the spanwise coherent vortices, bottom shear stress on overlying flow and shear stress on the ripple surface are identified as the key fluid dynamical controls in selecting the equilibrium dimensions of vortex ripples. Through the triple decomposition of the flow, the component of ripple-induced fluctuation is found to carry most of the controls, and its interaction with the other two components is also studied.

The turbulent oscillatory flow over vortex ripples is characterized by the periodic generation and ejection of columnar coherent vortices in a boundary layer close to the rippled bed. Detected using the method of vortex vector, in all four numerical cases, coherent vortices are formed at the lee side of ripples due to the separation of the flow from ripple crests, which become stronger as the flow decelerates. During the vortex-generation stage, how far a primary vortex can travel to the adjacent ripple is clearly affected by the ripple wavelength. For long ripples, the primary vortex cannot reach the ripple trough, but it can travel beyond the trough for short ripples. Meanwhile, as these vortices locate very close to the rippled bed in this stage, clear footprints indicated by the shear stress are left

on the ripple surface because of the intense vortex–bedform interaction. Around the phase of flow reversal, these lee vortices are ejected from ripple crests into the water column and move horizontally towards the neighbouring ripples until their disappearance. The strength of coherent vortices is quantified by the magnitude of the spanwise vorticity and vortex vector, which is significantly affected by the ripple height. As the ripple height increases, the resulting vortex strength becomes much stronger. The idea of the vortex influence zone turns out to be useful and intuitive for measuring the variation in trajectory and strength of spanwise coherent vortices caused by the disequilibrium ripple dimensions.

The bottom shear stress on overlying flow and the shear stress on the ripple surface play a role in selecting vortex ripple dimensions, regarding their implied role in the exchange of sediment with the rippled bed and the transport of sediment after being eroded. The bottom shear stress on overlying flow is conventionally divided into two components of skin friction and form drag. The component of form drag dominates the total bottom shear stress, where two peaks are found during the half-cycle of a wave period corresponding to the generation and ejection of the primary vortex, respectively. This is illustrated using the turbulence-averaged flow fields at the two instants when the dynamic pressure closely attaches to the ripple surface. The shear stress on the ripple surface is quantified by its magnitude, where clear footprints of primary vortices are found during the vortex-formation stage. After vortex ejection, an enhancement in the shear stress located on one side of ripple flank close to ripple crest is found. This enhancement of shear stress on ripple surface is of most practical interest, and is found to be caused by the accelerating upstream boundary layer flow covering the stoss-side ripple flank. Increase in ripple height or change in ripple wavelength from its equilibrium will cause an enhanced time-averaged resistance on the overlying flow and shearing felt by the ripple surface.

According to our findings from limited simulations, we propose a possible mechanism in the selection of vortex ripple dimensions (height and wavelength) or governing parameters (s and K_C) based on the strength of the coherent vortex and shear stress on the ripple surface. The latter can also be represented by flow resistance. That is, during the selection process of ripple dimensions, the interaction between overlying flow and vortex ripples tends to generate stronger coherent vortices while the ripple surface prefers smaller shear stress.

After the triple decomposition of the flow, we find that the component of ripple-induced fluctuation carries most of the fluid dynamical controls. In practice, the selection of vortex ripple height and wavelength actually happens simultaneously, characterized by the trajectory of coherent vortices and the corresponding signature in shear stress on ripple surface. Therefore, there is an evident advantage in investigating the ripple-induced fluctuation for our understanding of the selection process.

Admittedly, the sediment transport process is not modelled in this work, which should be important in determining the scales of equilibrium vortex ripples. However, from the study of clear flow over out-of-equilibrium vortex ripples, we first target the significant fluid dynamical controls in selecting vortex ripple dimensions. Based on our analysis, a possible selection mechanism is also proposed. Since our analysis on sediment transport is purely based on bed shear stress, the proposed selection process may be limited by the more energetic flow condition where the suspended load becomes dominant. Through the triple decomposition of the flow, the importance of ripple-induced fluctuation is emphasized. Our findings could improve the understanding of the formation of equilibrium vortex ripples and provide very useful guides for future work. To validate our findings, well-controlled laboratory experiments and high-accuracy measurements are warranted.

Acknowledgements. L.Y. thanks Dr A. Önder for providing the numerical data reported in Önder & Yuan (2019), which has been used in the model validation. Numerical simulations presented in this study were carried out using the Canviness cluster at the University of Delaware, and the Comet cluster at San Diego Supercomputer Center via XSEDE (TG-OCE100015).

Funding. This work was supported by the National Science Foundation (grant number OCE-1537231, OCE-1924532 and OCE-1537435).

Declaration of interests. The authors report no conflict of interest.

Author ORCIDs.
Liangyi Yue https://orcid.org/0000-0001-7421-8078;
Tian-Jian Hsu https://orcid.org/0000-0002-8473-3441;
Alexander R. Horner-Devine https://orcid.org/0000-0003-2323-7150.

References

VAN DER A, D.A., RIBBERINK, J.S., VAN DER WERF, J.J., O'DONOGHUE, T., BUIJSROGGE, R.H. & KRANENBURG, W.M. 2013 Practical sand transport formula for non-breaking waves and currents. *Coast. Engng* **76**, 26–42.

ANDERSEN, K.H., CHABANOL, M.-L. & VAN HECKE, M. 2001 Dynamical models for sand ripples beneath surface waves. *Phys. Rev.* E **63**, 066308.

AYRTON, H. 1910 The origin and growth of ripple-mark. *Proc. R. Soc. Lond.* A **84** (571), 285–310.

BAGNOLD, R.A. & TAYLOR, G.I. 1946 Motion of waves in shallow water. Interaction between waves and sand bottoms. *Proc. R. Soc. Lond.* A **187** (1008), 1–18.

BLACK, K.P. & OLDMAN, J.W. 1999 Wave mechanisms responsible for grain sorting and non-uniform ripple distribution across two moderate-energy, sandy continental shelves. *Mar. Geol.* **162** (1), 121–132.

BLONDEAUX, P. 2001 Mechanics of coastal forms. *Annu. Rev. Fluid Mech.* **33** (1), 339–370.

BLONDEAUX, P., SCANDURA, P. & VITTORI, G. 2004 Coherent structures in an oscillatory separated flow: numerical experiments. *J. Fluid Mech.* **518**, 215–229.

BUCKLEY, M.P. & VERON, F. 2019 The turbulent airflow over wind generated surface waves. *Eur. J. Mech. (B/Fluids)* **73**, 132–143.

CHARRU, F., ANDREOTTI, B. & CLAUDIN, P. 2013 Sand ripples and dunes. *Annu. Rev. Fluid Mech.* **45** (1), 469–493.

CHARRU, F. & FRANKLIN, E.M. 2012 Subaqueous Barchan dunes in turbulent shear flow. Part 2. Fluid flow. *J. Fluid Mech.* **694**, 131–154.

CHENG, Z., YU, X., HSU, T.-J., OZDEMIR, C.E. & BALACHANDAR, S. 2015 On the transport modes of fine sediment in the wave boundary layer due to resuspension/deposition: a turbulence-resolving numerical investigation. *J. Geophys. Res.* **120** (3), 1918–1936.

DAVIS, J.P., WALKER, D.J., TOWNSEND, M. & YOUNG, I.R. 2004 Wave-formed sediment ripples: transient analysis of ripple spectral development. *J. Geophys. Res.* **109**, C07020.

DIMAS, A.A. & LEFTHERIOTIS, G.A. 2019 Mobility parameter and sand grain size effect on sediment transport over vortex ripples in the orbital regime. *J. Geophys. Res.* **124** (1), 2–20.

DU TOIT, C.G. & SLEATH, J.F.A. 1981 Velocity measurements close to rippled beds in oscillatory flow. *J. Fluid Mech.* **112**, 71–96.

ELGAR, S., GUZA, R.T., RAUBENHEIMER, B., HERBERS, T.H.C. & GALLAGHER, E.L. 1997 Spectral evolution of shoaling and breaking waves on a barred beach. *J. Geophys. Res.* **102** (C7), 15797–15805.

FRANK-GILCHRIST, D.P., PENKO, A. & CALANTONI, J. 2018 Investigation of sand ripple dynamics with combined particle image and tracking velocimetry. *J. Atmos. Ocean. Technol.* **35** (10), 2019–2036.

GAO, Y. & LIU, C. 2018 Rortex and comparison with eigenvalue-based vortex identification criteria. *Phys. Fluids* **30** (8), 085107.

GRANT, W.D. & MADSEN, O.S. 1986 The continental-shelf bottom boundary layer. *Annu. Rev. Fluid Mech.* **18** (1), 265–305.

HARA, T. & SULLIVAN, P.P. 2015 Wave boundary layer turbulence over surface waves in a strongly forced condition. *J. Phys. Oceanogr.* **45** (3), 868–883.

HARE, J., HAY, A.E., ZEDEL, L. & CHEEL, R. 2014 Observations of the space-time structure of flow, turbulence, and stress over orbital-scale ripples. *J. Geophys. Res.* **119** (3), 1876–1898.

LONGUET-HIGGINS, M.S. 1981 Oscillating flow over steep sand ripples. *J. Fluid Mech.* **107**, 1–35.

MADSEN, O.S. 1994 Spectral wave-current bottom boundary layer flows. In *Proceedings of the 24th International Conference on Coastal Engineering, Kobe, Japan* (ed. B.L. Edge), vol. 1, pp. 384–398. American Society of Civil Engineers.

NAYAK, A.R., LI, C., KIANI, B.T. & KATZ, J. 2015 On the wave and current interaction with a rippled seabed in the coastal ocean bottom boundary layer. *J. Geophys. Res.* **120** (7), 4595–4624.

NELSON, K.S. & FRINGER, O.B. 2018 Sediment dynamics in wind wave-dominated shallow-water environments. *J. Geophys. Res.* **123** (10), 6996–7015.

NELSON, T.R. & VOULGARIS, G. 2014 Temporal and spatial evolution of wave-induced ripple geometry: regular versus irregular ripples. *J. Geophys. Res.* **119** (2), 664–688.

NELSON, T.R. & VOULGARIS, G. 2015 A spectral model for estimating temporal and spatial evolution of rippled seabeds. *Ocean. Dyn.* **65** (2), 155–171.

NELSON, T.R., VOULGARIS, G. & TRAYKOVSKI, P. 2013 Predicting wave-induced ripple equilibrium geometry. *J. Geophys. Res.* **118** (6), 3202–3220.

NICHOLS, C.S. & FOSTER, D.L. 2007 Full-scale observations of wave-induced vortex generation over a rippled bed. *J. Geophys. Res.* **112**, C10015.

NICHOLS, C.S. & FOSTER, D.L. 2009 Observations of bed form evolution with field-scale oscillatory hydrodynamic forcing. *J. Geophys. Res.* **114**, C08010.

NIELSEN, P. 1981 Dynamics and geometry of wave-generated ripples. *J. Geophys. Res.* **86** (C7), 6467–6472.

NIENHUIS, J.H., PERRON, J.T., KAO, J.C.T. & MYROW, P.M. 2014 Wavelength selection and symmetry breaking in orbital wave ripples. *J. Geophys. Res.* **119** (10), 2239–2257.

O'DONOGHUE, T., DOUCETTE, J.S., VAN DER WERF, J.J. & RIBBERINK, J.S. 2006 The dimensions of sand ripples in full-scale oscillatory flows. *Coast. Engng* **53** (12), 997–1012.

ÖNDER, A. & YUAN, J. 2019 Turbulent dynamics of sinusoidal oscillatory flow over a wavy bottom. *J. Fluid Mech.* **858**, 264–314.

OZDEMIR, C.E., HSU, T.-J. & BALACHANDAR, S. 2010 A numerical investigation of fine particle laden flow in an oscillatory channel: the role of particle-induced density stratification. *J. Fluid Mech.* **665**, 1–45.

PEDOCCHI, F. & GARCÍA, M.H. 2009 Ripple morphology under oscillatory flow: 1. Prediction. *J. Geophys. Res.* **114**, C12014.

VAN RIJN, L.C. 2007 Unified view of sediment transport by currents and waves. I: initiation of motion, bed roughness, and bed-load transport. *ASCE J. Hydraul. Engng* **133** (6), 649–667.

REYNOLDS, W.C. & HUSSAIN, A.K.M.F. 1972 The mechanics of an organized wave in turbulent shear flow. Part 3. Theoretical models and comparisons with experiments. *J. Fluid Mech.* **54** (2), 263–288.

RIBBERINK, J.S. & AL-SALEM, A.A. 1994 Sediment transport in oscillatory boundary layers in cases of rippled beds and sheet flow. *J. Geophys. Res.* **99** (C6), 12707–12727.

RIBBERINK, J.S., VAN DER WERF, J.J., O'DONOGHUE, T. & HASSAN, W.N.M. 2008 Sand motion induced by oscillatory flows: sheet flow and vortex ripples. *J. Turbul.* **9**, N20.

RODRÍGUEZ-ABUDO, S. & FOSTER, D.L. 2014 Unsteady stress partitioning and momentum transfer in the wave bottom boundary layer over movable rippled beds. *J. Geophys. Res.* **119** (12), 8530–8551.

SALIMI-TARAZOUJ, A., HSU, T.-J., TRAYKOVSKI, P. & CHAUCHAT, J. 2021 Eulerian two-phase model reveals the importance of wave period in ripple evolution and equilibrium geometry. *J. Geophys. Res.* **126** (7), e2021JF006132.

SCHERER, M.A., MELO, F. & MARDER, M. 1999 Sand ripples in an oscillating annular sand-water cell. *Phys. Fluids* **11** (1), 58–67.

SCHERER, M., UHLMANN, M., KIDANEMARIAM, A.G. & KRAYER, M. 2022 On the role of turbulent large-scale streaks in generating sediment ridges. *J. Fluid Mech.* **930**, A11.

SCULLY, M.E., TROWBRIDGE, J.H., SHERWOOD, C.R., JONES, K.R. & TRAYKOVSKI, P. 2018 Direct measurements of mean Reynolds stress and ripple roughness in the presence of energetic forcing by surface waves. *J. Geophys. Res.* **123** (4), 2494–2512.

SISHAH, B. & VITTORI, G. 2022 RANSE modeling of the oscillatory flow over two-dimensional rigid ripples. *J. Geophys. Res.* **127** (1), e2021JC017439.

SPALART, P.R. & BALDWIN, B.S. 1989 Direct simulation of a turbulent oscillating boundary layer. In *Turbulent Shear Flows 6* (ed. J.-C. André, J. Cousteix, F. Durst, B.E. Launder, F.W. Schmidt & J.H. Whitelaw), pp. 417–440. Springer.

SULLIVAN, P.P., MCWILLIAMS, J.C. & MOENG, C.H. 2000 Simulation of turbulent flow over idealized water waves. *J. Fluid Mech.* **404**, 47–85.

TIAN, S., FU, H., XIA, J. & YANG, Y. 2020 A vortex identification method based on local fluid rotation. *Phys. Fluids* **32** (1), 015104.

TIAN, S., GAO, Y., DONG, X. & LIU, C. 2018 Definitions of vortex vector and vortex. *J. Fluid Mech.* **849**, 312–339.

TRAYKOVSKI, P. 2007 Observations of wave orbital scale ripples and a nonequilibrium time-dependent model. *J. Geophys. Res.* **112**, C06026.

TRAYKOVSKI, P., HAY, A.E., IRISH, J.D. & LYNCH, J.F. 1999 Geometry, migration, and evolution of wave orbital ripples at LEO-15. *J. Geophys. Res.* **104** (C1), 1505–1524.

TROWBRIDGE, J.H. & LENTZ, S.J. 2018 The bottom boundary layer. *Ann. Rev. Mar. Sci.* **10** (1), 397–420.

WANG, D. & YUAN, J. 2018 Bottom-slope-induced net sediment transport rate under oscillatory flows in the rippled-bed regime. *J. Geophys. Res.* **123** (10), 7308–7331.

WANG, D. & YUAN, J. 2019 Geometric characteristics of coarse-sand ripples generated by oscillatory flows: a full-scale experimental study. *Coast. Engng* **147**, 159–174.

WANG, D. & YUAN, J. 2020 An experimental study of net sediment transport rate due to acceleration-skewed oscillatory flows over rippled seabeds. *Coast. Engng* **155**, 103583.

VAN DER WERF, J.J., DOUCETTE, J.S., O'DONOGHUE, T. & RIBBERINK, J.S. 2007 Detailed measurements of velocities and suspended sand concentrations over full-scale ripples in regular oscillatory flow. *J. Geophys. Res.* **112**, F02012.

VAN DER WERF, J.J., MAGAR, V., MALARKEY, J., GUIZIEN, K. & O'DONOGHUE, T. 2008 2DV modelling of sediment transport processes over full-scale ripples in regular asymmetric oscillatory flow. *Cont. Shelf Res.* **28** (8), 1040–1056.

WIBERG, P.L. & HARRIS, C.K. 1994 Ripple geometry in wave-dominated environments. *J. Geophys. Res.* **99** (C1), 775–789.

YANG, D. & SHEN, L. 2010 Direct-simulation-based study of turbulent flow over various waving boundaries. *J. Fluid Mech.* **650**, 131–180.

YANG, D. & SHEN, L. 2011 Simulation of viscous flows with undulatory boundaries. Part I: basic solver. *J. Comput. Phys.* **230** (14), 5488–5509.

YUAN, J. & WANG, D. 2018 Experimental investigation of total bottom shear stress for oscillatory flows over sand ripples. *J. Geophys. Res.* **123** (9), 6481–6502.

YUAN, J. & WANG, D. 2019 An experimental investigation of acceleration-skewed oscillatory flow over vortex ripples. *J. Geophys. Res.* **124** (12), 9620–9643.

YUE, L. 2020 Turbulence-resolving numerical investigations of coastal bottom boundary layer and fine sediment transport. PhD thesis, University of Delaware, Newark, DE.

YUE, L., CHENG, Z. & HSU, T.-J. 2019 Turbid: a turbulence-resolving numerical model for simulating bottom boundary layer and fine sediment transport. *Tech. Rep.* Center for Applied Coastal Research, Department of Civil and Environmental Engineering, University of Delaware, Newark, DE.

YUE, L., CHENG, Z. & HSU, T.-J. 2020 A turbulence-resolving numerical investigation of wave-supported gravity flows. *J. Geophys. Res.* **125** (2), e2019JC015220.

ZHANG, W.Y., HUANG, W.X. & XU, C.X. 2019 Very large-scale motions in turbulent flows over streamwise traveling wavy boundaries. *Phys. Rev. Fluids* **4** (5), 054601.

ZHOU, J., ADRIAN, R.J., BALACHANDAR, S. & KENDALL, T.M. 1999 Mechanisms for generating coherent packets of hairpin vortices in channel flow. *J. Fluid Mech.* **387**, 353–396.